



Layered gabbros and peridotites from Piton des Neiges volcano, La Réunion Island

C. Berthod, Laurent Michon, V. Famin, B. Welsch, P. Bachèlery, J. Bascou

► To cite this version:

C. Berthod, Laurent Michon, V. Famin, B. Welsch, P. Bachèlery, et al.. Layered gabbros and peridotites from Piton des Neiges volcano, La Réunion Island. *Journal of Volcanology and Geothermal Research*, 2020, 405, pp.107039. 10.1016/j.jvolgeores.2020.107039 . hal-02942660

HAL Id: hal-02942660

<https://uca.hal.science/hal-02942660>

Submitted on 14 Sep 2022

HAL is a multi-disciplinary open access archive for the deposit and dissemination of scientific research documents, whether they are published or not. The documents may come from teaching and research institutions in France or abroad, or from public or private research centers.

L'archive ouverte pluridisciplinaire **HAL**, est destinée au dépôt et à la diffusion de documents scientifiques de niveau recherche, publiés ou non, émanant des établissements d'enseignement et de recherche français ou étrangers, des laboratoires publics ou privés.



Distributed under a Creative Commons Attribution - NonCommercial 4.0 International License

Layered gabbros and peridotites from Piton des Neiges volcano, La Réunion Island

C. Berthod^{1,2,3*}, L. Michon^{2,3}, V. Famin^{2,3}, B. Welsch⁴, P. Bachèlery¹, J. Bascou⁵

¹Université Clermont Auvergne, CNRS, IRD, OPGC, Laboratoire Magmas et Volcans, 6 avenue
Blaise Pascal, 63178 Aubière, France.

²Université de La Réunion, Laboratoire GéoSciences Réunion, F-97744 Saint Denis, France.

³Université de Paris, Institut de physique du globe de Paris, CNRS, F-75005 Paris, France.

⁴University of Hawaii–Manoa, Department of Earth Sciences, 1680 East-West Road 96822 Honolulu,
Hawaii, USA.

⁵Université de Lyon, Université Jean Monnet and UMR-CNRS 6524, Laboratoire Magmas et
Volcans, 42023 Saint-Etienne, France

**Corresponding author: carole.berthod@uca.fr;*

C. Berthod 0000-0001-6890-5541

L. Michon 0000-0002-4486-5378

V. Famin 0000-0001-7451-5363

B. Welsch

P. Bachèlery 0000-0002-0108-5486

J. Bascou 0000-0002-9357-6951

Highlights

- Layered gabbros and peridotites outcrop in the cirque of Salazie (Piton des Neiges).
- Plutonic rocks are parts of a large composite plutonic complex.
- Peridotitic and gabbroic bodies were active at different periods of time.
- Plutonic bodies were made by incremental stacking of independent magma intrusions.
- The proto summit of Piton des Neiges was located north of its current position

Keywords: La Réunion, Piton des Neiges, shield volcano, plutonic complex, layered intrusion, gabbro, peridotite.

ABSTRACT

We conducted a petrological study of the layered gabbros and peridotites outcropping in the cirque of Salazie, combining field investigations, geochemistry, petrography and, mineralogy to constrain the magmatic evolution of Piton des Neiges volcano (La Réunion). Three new hectometer-long outcrops are reported here (Sites 1, 2 and 3) in addition to the gabbroic series (hereafter named Site 4) previously described in the literature. The Sites 1 and 2 are located in the upper parts of the Mât River and show dunite and wehrlite units with no apparent foliation, lineation, or layering. The Sites 3 and 4 are located in the lower parts of the river and are made of olivine-gabbro, gabbro and ferrogabbro units showing marked foliation and lineation, and abundant layering. The mean composition of primary phases varies between Sites 1–2 and Sites 3–4: $Fo_{89.5}$ to $Fo_{69.8}$ in olivine, Mg# of 90 to 69 in clinopyroxene, and Mg# of 44 to 0 in Cr-spinel, titanomagnetite and, ilmenite, respectively. Here we show that the layered gabbros and peridotites exposed at the four sites represent multiple levels of magma storage. Based on the results of previous gravimetric studies and a drill hole related to geothermal exploration, we propose that the gabbroic series belongs to a magmatic system predating the building of Piton des Neiges and centered underneath the cirque of Salazie. The high volume of erupted materials in the NE quadrant of the volcanic edifice, and the southward magmatic flow direction in the layered gabbros suggest that the initial eruptive center of Proto-Piton des Neiges was above the cirque of Salazie, ~3 km north of the present-day summit. The landscape of Piton des Neiges may have changed when its NE flank experienced a major lateral collapse, after complete solidification of the gabbroic bodies. The magmatic activity, then, shifted southward after the flank collapse. Finally, we suggest that peridotites outcrops are associated with the present-day Piton des Neiges.

1 Introduction

Fossil magma chambers are remarkable archives of volcanic systems throughout their lifetime. Magma chambers supplying volcanoes are characterized by partially or entirely molten rock carrying various proportions of crystals, and gradually lose heat and crystallize inwards from their margins (Marsh 2006; Cashman et al. 2017; Jackson et al. 2018; Sparks et

al. 2019; Edmonds et al. 2019). Crustal magma bodies are commonly formed and grown by incremental injections of new magma from depth (Deniel et al. 1987; Annen and Sparks 2002; Glazner et al. 2004; Gudmundsson 2012; Annen et al. 2015; Blundy and Annen 2016; Karakas et al. 2017; Cashman et al. 2017; Sparks et al. 2019). Their internal structures record the compositional evolution, transport dynamics, and mode of crystallization in these systems, while their external structures (size, geometry) are imprints of the storage level, and the volume and frequency of magma transfers (Marsh 2006; Szymanowski et al. 2017; Jackson et al. 2018; Sparks et al. 2019; Edmonds et al. 2019). Having access to such records is critical not only in reconstructing the history of a given volcano, but also in assessing its past behavior and those of other edifices built from the same mantle source.

Probing such systems is, however, a challenge as magma chambers reside deep in the crust and rarely outcrop in active contexts. Similarly to Fuerteventura (Canary Islands; Allibon et al., 2011; Tornare et al., 2016), La Réunion has the advantage of extreme erosion rates (Gayer et al. 2019) providing access to plutonic outcrops related to major volcanic edifices, including one active. Taking La Réunion as one of the archetypes of mafic magmatism and shield volcanism, this contribution focuses on four outcrops of plutonic rocks in the cirque of Salazie; three are newly discovered during our fieldwork along the Mât River. We report here field observations and the mineralogy, petrography and geochemistry for these outcrops in order to constrain the structure of igneous bodies and the magma processes at work in the past activity of Piton des Neiges volcano. These results are placed in the context of the morphological and structural evolution of the volcano, with implications on the magmatic activity of the igneous system.

2 Geological setting

La Réunion is a volcanic island located in the western Indian Ocean, at 700 km east of Madagascar (Fig.1). The island is the current manifestation of the hotspot that produced the Deccan Traps at the K-T boundary, but also intermediately a chain of age-decreasing volcanic constructions consisting of Laccadives, Maldives, Chagos, the Mascarene plateau, and Mauritius (Duncan et al. 1989; Mahoney et al. 2002; Courtillot et al. 2003). Based on radiometric dating of subaerial rocks, current effusive rates and volumetric estimates of the island, La Réunion is thought to be active since at least 5 Ma (Gillot et al. 1994; Lénat et al. 2001) with the edification of two successive shield volcanoes (Fig. 1a): Piton des Neiges, from > 2.2 to 0.029 Ma (McDougall 1971; Quidelleur et al. 2010; Salvany et al. 2012) and

Piton de la Fournaise, from > 0.53 Ma to these days (Gillot et al. 1994). A study of the morpho-structure of the island has shown that the whole edifice is essentially built by the old Piton des Neiges and that the formations of the younger Piton de la Fournaise represent only a small fraction on its eastern flank (Le Friant et al. 2011; Lebas et al. 2018). Piton de la Fournaise volcano is currently in its shield building stage and has been a mainstay for centuries as a natural laboratory for volcanological studies (Vincent 1804; Lacroix 1916; Lacroix 1923; Lacroix 1936). Piton des Neiges is dormant and an important source of information on the past magmatic and volcanic activity of La Réunion hotspot volcanoes. Previous studies have shown that magmas of Piton des Neiges evolved through time with the effusion of basalts and olivine-rich basalts during the shield stage from >2.2 to 0.43 Ma, then consecutive to a period of quiescence of 0.08 Ma, the eruption of plagioclase-rich basalts, hawaiites, mugearites, benmoreites, trachytes and comendites during the postshield stage from 0.35 to 0.029 Ma (Upton and Wadsworth 1966; Upton and Wadsworth 1967; McDougall 1971; Oversby 1972; Nativel 1978; Fisk et al. 1988; Gillot et al. 1994; Kluska 1997; Quidelleur et al. 2010; Smietana 2011; Salvany et al. 2012). The volcanic activity of Piton des Neiges fluctuated considerably during its long life, leading to the building of three successive basaltic shield edifices (before 2 Ma, between 1.4 and 0.95 Ma, and between 0.6 and 0.43 Ma) and two stratocones (between 0.35 and 0.18 Ma, and between 0.14 Ma and 0.029 Ma, McDougall 1971; Gillot and Nativel 1982; Salvany et al. 2012; Gayer et al. 2019).

The morphology of Piton des Neiges is dissected by three major topographic depressions, the cirques of Cilaos, Mafate, and Salazie, from which the internal structure of the volcano is now reachable. The cirque of Salazie has been found to host a plutonic body outcropping in the meanders of the Mât River (Lacroix 1923; Upton and Wadsworth 1972; Chevallier and Vatin-Perignon 1982), described hereafter as Site 4 (Fig. 1b-c). The top of this plutonic body, subjected to many structural studies, is a detachment that led to a northward destabilization of the northern flank of Piton des Neiges (Famin and Michon 2010; Chaput et al. 2014a; Chaput et al. 2014b; Berthod et al. 2016). This northward motion, associated with brittle-ductile deformation and low-temperature hydrothermal alteration (150 – 250 °C; Famin et al., 2016), occurred during shield building (Berthod 2016).

About 3 km North of Site 4, remnants of a plutonic body have been sampled by the SLZ1 geothermal drill hole (Fig. 1b), from 350 to 1314 m below sea level (bsl; Chovelon, 1986; Demange et al., 1989). These rocks consist of monzogabbros and gabbros (5.97 – 9.96 wt% MgO in bulk) between 350 and 795 m bsl, and olivine gabbros (30.1 wt% MgO in bulk)

below 795 m bsl. The bottom of the plutonic body is not intersected by the drill hole, but establishes a minimum thickness of 964 m. In parallel with these reports of plutonic rocks in the Mât River and the drill hole, gravimetric and magnetotelluric studies have documented the presence of a large, dense body underneath the volcano, extending from the subsurface down to 4000 m bsl (Malengreau et al. 1999; Gailler 2010; Gailler and Lénat 2012). Finally, another large plutonic body has been identified under the eastern parts of Piton de la Fournaise volcano by gravimetric and magnetotelluric campaigns (Rousset et al. 1989; de Voogd et al. 1999; Malengreau et al. 1999; Gailler et al. 2009; Gailler and Lénat 2010; Gailler 2010; Gailler and Lénat 2012). This plutonic body has been sampled by the SR1 geothermal drill hole (Fig 1a; Lerebour et al., 1989; Rançon et al., 1989; Augé et al., 1989; Rousset et al., 1989) and shown to comprise a succession of gabbros, wehrlites and dunites from top (838 m bsl) to bottom (2831 m bsl). Again, drilling does not reach the bottom of this body but establishes a minimum thickness of 1993m. Although this magma body has been related to submarine lava flows dated at 3.34 and 3.77 Ma (Smietana 2011), the intricacies of its relationships with the past activity of Piton de la Fournaise are still debated (Lénat et al. 2001; Le Friant et al. 2011; Lebas et al. 2018).

3 Field observations

We conducted new field investigations in the inner parts of Piton des Neiges volcano (Fig. 1a-b) and found three new outcrops of plutonic rocks in the cirque of Salazie along the upper course of the Mât River (hereafter labeled Site 1, Site 2 and Site 3, Fig. 1c), each hectometric to pluri-hectometric in size, and located upstream of the gabbroic series of Site 4 described in Upton and Wadsworth (1972). All the plutonic outcrops are crosscut by a network of clinopyroxene- and/or plagioclase-rich veinlets (Fig. 2a). The veinlets are centimetric to decimetric in thickness, and their complexity increases from Sites 1–2 to Sites 3–4. Prehnite-pumpellyite or lower greenschist facies alteration is observed at all sites, but is most apparent at Site 4. Taken together, the four outcrops occur within an area of 2.5 x 1.0 km and all present upper contacts with a pile of sills surmounted by a mafic breccia and crosscut by mafic dykes. These dykes consist of 0.5–1.5-m-thick olivine-rich basalt intrusions dipping 15–30° toward the North. Importantly, the current geometry, i.e. igneous bodies surmounted by sills and a breccia, results from one or several volcano flank destabilizations that likely occurred while the plutonic rocks were already solidified (Famin et al. 2016). The main

features of the four sites are described below.

3.1 Site 1

The plutonic rocks are located in the southernmost part of the area, upstream and at 950–1200 m above sea level (asl), i.e. at a higher elevation than the other plutonic outcrops (Fig. 1c). They are exposed along the river over an area of 600 m north-south and 200 m east-west for a maximum thickness of 250 m. The mass is composed of centimetric- to plurimetric-thick lenses of peridotite separated by mafic intrusions (Fig. 2b). No foliation nor lineation is observed.

3.2 Site 2

The plutonic rocks outcrop about 700 m downstream from Site 1, at 850–940 m asl. Their exposure spreads over 200 m in the direction north-south and 50 m east-west for a thickness of 15–20 m. The plutonic rocks at Site 2 consist of plurimetric-thick layers of peridotite with no apparent foliation or lineation, that gently dip ($<10^\circ$) toward the north and curve close to the downstream contact with the pile of sills (Fig. 2c). The layers are cut by fractures that produce a network of centimetric to pluri-metric lenses.

3.3 Site 3

The plutonic rocks outcrop about 900 m downstream of those at Site 2. They are exposed over an area of 90 m north-south by 200 m east-west for a thickness of about 20 m at elevations of 750–870 m asl. The eastern and western parts of the plutonic mass are crosscut by a pluri-hectometric syenite intrusion, as detailed in section §3.5. The plutonic rocks of Site 3 consist of a layered gabbro (Fig. 2d-e) with centimetric- to pluri-decimetric-thick layers and a N60 45°S magmatic foliation defined by variations in modal proportion and/or grain-size of olivine, clinopyroxene and plagioclase (Fig. 3). The gabbroic layers show a magmatic lineation with an average orientation N8 48°S (Fig. 3) outlined by pluri-millimetric to centimetric elongated crystals of clinopyroxene and plagioclase. The gabbroic layering is affected by SE-NW trending thrust syn-magmatic faults (Fig. 2d). Layering is ductilely deformed with structures that share similarities to slump structures in sedimentary rocks. These dynamic structures include west-verging overturned folds (Fig. 2e-f), centimetric lenticular schlierens, discontinuous layering, and rare mafic autholiths. The schlierens are generally made of plagioclase crystals and are mostly parallel to the layering.

3.4 Site 4

These plutonic rocks form the outcrop previously described by Upton and Wadsworth (1972). These rocks are exposed about 200 m downstream from those exposed at Site 3, past the syenite intrusion. The plutonic rocks of Site 4 outcrop between 660 and 750 m asl, over a distance of 300 m and, for a thickness of about 20 m. They consist of a fine-layered gabbro with a foliation oriented N92 44°S on average (Figs 2f-g, 3) similar to that observed at Site 3. Their layering tends to be thicker and laminar compared with those of the layered gabbro of Site 3, ranging from centimetric to metric in thickness (Fig. 2g). Similarly to Site 3, the magmatic lineation of the plutonic rocks of Site 4 is defined by the fabrics of elongated crystals of plagioclase and clinopyroxene, although scarcer and more dispersed than there, with an average orientation N212 43°S (Fig. 3). The fine layered gabbro is also affected by several E–W trending reverse faults. Dynamic structures such as slumps and cross beddings are locally observed (Fig. 2f). The northern limit of the gabbroic outcrop corresponds to a detachment fault, gently dipping northward, and in which mafic sills were intruded (Famin and Michon 2010).

3.5 Syenite intrusion

The syenite intrusion crosscuts the layered gabbros of Sites 3 and 4 (Fig. 1c) at 750–850 m asl, over an area of 200 m north-south by 300 m east-west in the Mât River. The second outcrop, located upstream Site 3, is exposed over an area of 200 m north-south by 20 m east-west. The intrusion is fine-grained and massive and thought to be emplaced during the differentiated stage of Piton de Neiges, i.e. with an age younger than 0.35 Ma (McDougall 1971). Unlike the layered gabbros, the syenite does not show any field evidence of prehnite-pumpellyite or lower greenschist facies alteration.

4 Samples & analytical methods

A multi-method approach was carried out to provide an integrated analysis of the four sites. A first set of 44 samples was collected for their petrographic examination (Tab. 1). Among them, 39 samples were used to determine *in situ* chemical compositions of the mineral phases present in the plutonic rocks. The analyses were performed using the CAMECA SX-100 electron microprobe analyzer (EPMA) of the *Laboratoire Magmas et Volcans* (Clermont-Ferrand, France). The beam was set at an accelerating potential of 15 kV and a probe current of 15 nA for major, minor and trace elements (Na, Al, Si, Ca, Fe, Mg, Ti, Mn, K, and P), with 10 s counting times for each element and 20 µm beam diameter. Routine calibration was

performed with a CAMECA set of natural and synthetic mineral standards: orthoclase (K), albite (Na), Al_2O_3 (Al) wollastonite (Si, Ca), fayalite (Fe), forsterite (Mg), TiMnO_3 (Ti, Mn), NiO (Ni), Cr_2O_3 (Cr). The same operating conditions were used for olivine, clinopyroxene, plagioclase, and oxides analysis. The second set of 19 samples was used for bulk rock major- and trace-element compositions (4, 2, 8, and 5 samples for Sites 1, 2, 3 and, 4, respectively). The analyses were performed in the Service d'Analyse des Roches et des Minéraux (SARM) at the *Centre de Recherches Pétrographiques et Géochimiques* (Nancy, France). Major elements concentrations were quantified with a Thermo Fischer ICap 6500 ICP-OES on three aliquots of whole-rock powders and completed with trace element analyses by a Thermo Elemental X7 ICP-MS. The samples were prepared for the analyses by fusion with LiBO_2 and dissolution with HNO_3 . Analytical uncertainty (1σ) is 1 – 15% for major elements and 5 – 15% for minor and trace elements.

5 Results

5.1 Rock types and textures

The representative parageneses and textures of samples are given in Figures 4, 5, and 6, and their modal compositions are given in Table 2. The samples collected at Sites 1 and 2 are peridotitic rocks consisting of dunites and wehrlites containing less than 10 vol% of plagioclase. In contrast, the samples collected at Sites 3 and 4 are principally gabbroic rocks, including olivine gabbros, gabbros, ferrogabbros and anorthosites containing more than 10 vol% of plagioclase. Overall the samples, we noted very little evidence of plastic deformation (such as kink-bands) in the minerals.

5.1.1 Dunites

Dunites are exclusively observed at Sites 1 and 2 where they represent 33% and 44% of the samples, respectively (Fig. 4). They present an adcumulate texture made of olivine (≥ 80 vol%), clinopyroxene (< 5 vol%), and minor oxides (Fig. 5a-b). The olivine crystals are euhedral to subhedral in shape and 0.5–1 cm in diameter and form a cumulus framework. The clinopyroxene crystals are on average smaller than olivines (0.1–1 cm in diameter) and are interstitial in the olivine fabric, with anhedral shapes. Oxide crystals include 10–50 μm Cr-spinel inclusions in the olivine crystals and small ilmenite crystals within the olivine

fractures. Olivine is often partly or entirely altered into serpentine and chlorite.

5.1.2 Wehrlites

The wehrlite samples of Sites 1 and 2 (67 % and 56 % of the samples, respectively; Fig. 4) present a heteradcumulate texture built on interlocking, poikilitic grains of clinopyroxene (15–40 vol%) enclosing crystals of olivine (55–80 vol%), plagioclase (<10 vol%) and oxides (<5 vol%; Fig. 5c-d). The clinopyroxene and olivine crystals are euhedral to subhedral and present a grain size of 0.1–10 mm and 0.2–5 mm, respectively. The oxides consist of euhedral 10–50 µm Cr-spinel inclusions in olivine and anhedral 5–200 µm titano-magnetite crystals enclosed in interstitial position. Three wehrlite samples from Site 2 (CB1230513, CB2230513, and CB4230513 in Table 2) show anhedral to euhedral crystals of plagioclase and sector-zoned clinopyroxene enclosing rounded crystals of olivine (Fig. 5e-f). The wehrlite sample of Site 4 (Fig. 4) presents an adcumulate texture made of 1–3 mm diameter, subhedral to euhedral crystals of olivine and clinopyroxene. The olivine and clinopyroxene crystals are in cumulus and interstitial position, respectively. The plagioclase crystals are interstitial, and 0.3–3 mm in diameter with a subhedral to anhedral shape. The magnetite and ilmenite crystals occur as intergrowths homogeneously distributed in the rock with a grain size of 20–300 µm in diameter. Similarly to the dunites, the olivine crystals in the wehrlites can be partly or entirely altered into serpentine and chlorite, with secondary titano-magnetite in the fractures (Fig. 5e, g). Plagioclase is locally altered into sericite.

5.1.3 Olivine gabbros

Olivine gabbro is a dominant lithology at Site 4 (70% of the samples; Fig. 4). In contrast, it represents 25% of the samples collected in Site 3. The samples are mesocumulates to adcumulates made of cumulus crystals of olivine (2–45 vol%) and clinopyroxene (39–55 vol%) embedded in interstitial plagioclase (15–49 vol%) and oxides (Fig. 6a-b). The crystals of olivine and clinopyroxene are subhedral to euhedral and > 1 mm in diameter, except for one sample (SAL111) in which the olivine crystals are euhedral and in interstitial position. Plagioclase occurs in the olivine gabbro samples as large crystals (0.4 to 1 mm) with anhedral to euhedral shapes and both cumulus and interstitial positions. The oxide crystals consist of intergranular titano-magnetite intergrowth with ilmenite, homogeneously distributed in the rock. Minor phlogopite (< 1 vol%) occur as small anhedral crystals (< 100 µm) in association with clinopyroxene and plagioclase. Olivine displays various degrees of iddingsitization, most

apparent at Site 4. Clinopyroxene can be partly or entirely replaced by uralitic amphibole and chlorite. Plagioclase may be altered into sericite and albite. Successive mineralization of prehnite, zeolite, and calcite are observed in fissures.

5.1.4 Gabbros

The gabbro rock type represents 25 and 15% of the samples collected at Sites 3 and 4, respectively (Fig. 4). The samples display an adcumulate to mesocumulate texture characterized by fine-grained crystals of clinopyroxene (44–80 vol%; Fig. 6c-d) and plagioclase (20–54 vol%). The clinopyroxene crystals are in cumulus position and have a stubby shape and a grain size in the range 0.05–0.3 mm. Plagioclase crystals are subhedral to euhedral tablets in cumulus or interstitial position with a grain size ranging from 0.2 to 1 mm, defining a strong fabric. The samples contain also minor oxides (1–5 vol%) consisting in intergrown crystals of titanomagnetite and ilmenite. As for olivine gabbros, magmatic minerals locally show evidence of uralitic and/or sericitic alteration.

5.1.5 Ferrogabbros

The ferrogabbros of Site 3 (42% of the samples) and Site 4 (10%) have a texture similar to the above-mentioned gabbro samples, except that they contain up to 5 vol% of Fe-Ti oxides crystals in cumulus and interstitial position and a lower abundance of clinopyroxene and plagioclase in cumulus and interstitial position (25–50 vol% and 40–45 vol%, respectively; Fig. 6e–f). Several samples display a slightly greater range of grain sizes but are not distinctly porphyritic in appearance. The clinopyroxene crystals present also a stubby shape with a grain size in the range 0.05–0.3 mm. Plagioclase shows a tabular shape and a grain size of 0.2–1 mm that define, in some cases, a strong fabric (Fig. 6e–f). Local alteration is similar to that of other gabbros.

5.1.6 Anorthosites

The anorthosites occur only as veinlets that crosscut the plutonic masses at Sites 1, 2, 3, and 4. The samples collected at Site 3 are made of cumulus crystals of plagioclase (~ 96 vol%), clinopyroxene (~ 3 vol%), and sparse Fe-Ti oxide (< 1 vol%) forming an adcumulate texture. The plagioclase and clinopyroxene crystals show euhedral to subhedral shapes with a grain size ranging from 0.1 to 1.5 mm. Anorthosites are locally altered into assemblages of chlorite + sericite + albite + zeolite ± calcite.

5.1.7 Syenite

The syenite intrusion crosscutting Sites 3 and 4 is composed of sub-euhedral alkali feldspar (< 10 vol%, <500 μ m) and amphibole (<1 vol%, up to 5 mm) macrocrysts, embedded in a groundmass containing microcrysts of elongated plagioclases, sodic pyroxenes, and Fe-Ti oxides. Unlike the layered gabbros, the syenite can be vesicular. Vesicles are filled with calcite.

5.2 Chemical composition of minerals

Representative chemical compositions of olivine, clinopyroxene, plagioclase, and oxides are given in Tables 3–6 and plotted in Figures 7–10. Compositional zoning is weak or absent in the samples, hence only representative compositions were reported for each mineral.

5.2.1 Olivine

The data given in Table 3 and Figure 7 indicate that two olivine groups can be distinguished based on their Fo content: Fo-rich olivine at $Fo_{>81}$ in the peridotites of Site 1 ($Fo_{84.1-87.9}$) and Site 2 ($Fo_{81-89.5}$), and Fe-rich olivine at $Fo_{<80}$ in the gabbros of Site 3 ($Fo_{75.2-76.4}$) and Site 4 ($Fo_{69.8-79.3}$). Among the Fo-rich group, the olivine grains in the dunites present a scattered Fo distribution with a mode at $Fo_{82.5}$ (in samples from Site 2) and two other main populations at $Fo_{87.5-88}$ (Sites 1 and 2) and $Fo_{89.0-89.5}$ (Site 2 only; Fig. 7). The wehrlites show similar olivine compositions to the dunites but with the main mode around $Fo_{85.5}$ (Fig. 7). The olivine composition at $Fo_{89.5}$ in dunite from Site 2 represents one of the highest Fo content measured in the subaerial domain of La Réunion, after the highest value at $Fo_{90.6}$ reported by Sobolev and Nikogosian for olivine of Piton des Neiges (1994). Among the Fe-rich olivine group, three populations can be observed in the olivine gabbros of Sites 3 and 4: the main mode at Fo_{73-77} and two less represented populations at $Fo_{70-70.5}$ and $Fo_{78.5-79}$ (Fig. 7). It is important to note that interstitial olivine has a composition similar to cumulus olivine.

The CaO contents of olivine, plotted in Figure 7b, may be classified into three populations: (1) a low CaO (0.05–0.20 wt%), high Fo_{84-89} population in dunites and wehrlites from Sites 1 and 2; (2) a high CaO (0.20–0.40 wt%), high Fo_{80-89} population only found in the dunites and wehrlites of Site 2; (3) A low CaO (~0.01–0.12 wt%), low Fo_{70-79} population in the wehrlite and olivine gabbros of Sites 3 and 4. Importantly, the olivine grains of the population (2) show rounded contours in the wehrlites (Fig. 5e-h) and their compositions are similar to that of olivine-bearing lavas erupted at Piton de la Fournaise (Boudoire et al. 2019).

5.2.2 Clinopyroxene

Clinopyroxene compositions are presented in Figure 8. A correlation is observed between the Mg# of clinopyroxenes and the rock, as the most mafic rocks (Sites 1 and 2) contain high-Mg# clinopyroxenes whereas evolved rocks (Sites 3, 4) contain lower Mg# clinopyroxenes (Fig. 8a). The clinopyroxene crystals of Site 1 consist of $\sim\text{En}_{48}\text{Fs}_7\text{Wo}_{45}$ diopside at Mg# = 86–89, with 0.03–1.18 wt% Cr_2O_3 and 3.37–3.70 wt% Al_2O_3 (Tab. 4, Fig. 8a, b, and c). The clinopyroxene crystals of Site 2 have more variable compositions at $\text{En}_{38-49}\text{Fs}_{5-17}\text{Wo}_{39-48}$ and Mg# = 69–90 spread over the fields of diopside and augite, with Cr_2O_3 contents ranging from below the detection limit to 1.41 wt% and Al_2O_3 contents at 1.07–5.99 wt%. These variations might correspond to sector zoning observed in some samples (Fig. 5g-h). Clinopyroxene crystals at Site 3 are also diopside/augite at $\text{En}_{40-46}\text{Fs}_{8-16}\text{Wo}_{40-47}$, with a Mg# at 73–84, Cr_2O_3 ranging from below the detection limit to 0.69 wt% and Al_2O_3 from 0.99 to 5.18 wt%. The clinopyroxene crystals of Site 4 are diopside/augite at $\text{En}_{40-46}\text{Fs}_{7-15}\text{Wo}_{42-49}$ with Mg# in the range 73–86, less than 0.55 wt% Cr_2O_3 , and 0.88 to 8.07 wt% Al_2O_3 . It is important to note that the Cr_2O_3 content of clinopyroxene decreases with the Mg# from the peridotites of Sites 1 and 2 to the gabbroic rocks of Sites 3 and 4 (Fig. 8b).

5.2.3 Plagioclase

As a general observation, the composition of plagioclase is bimodal in the layered gabbros and peridotites, with a high anorthite population (An_{65-81}) observed at Sites 1, 3, 4, and a lower anorthite population ($\leq \text{An}_{65}$) found at Sites 2, 3, 4 (Fig. 9a). The plagioclase crystals occurring in the anorthosite veinlets of Site 1 have a composition at $\text{An}_{77-82}\text{Ab}_{18-22}\text{Or}_{0.4-0.9}$ (Tab. 5). The plagioclase crystals of the wehrlites of Site 2 show chemical compositions that are either intermediate ($\sim \text{An}_{57}$) or albitic ($\sim \text{An}_{06}$), a probable result of late alteration. The plagioclase crystals of Site 3 are An_{51-82} grains with some albitic individuals at An_{14-23} (gabbro sample CB7230513). The plagioclase crystals of Site 4 occur mainly as An_{47-87} grains. Plotted in K_2O vs. An space (Fig. 9b), the K_2O content of plagioclase increases overall from 0.07–0.16 wt% at Site 1, to 0.12–0.35 wt% to Site 2, and to 0.03–0.64 wt% at Sites 3 and 4. We note that the composition range at $\text{An}_{75.3-82.2}$ of plagioclase in the anorthositic veinlets of the Site 3 is similar to that of the plagioclase crystals observed in the anorthositic veinlets of the Site 1.

383

384 5.2.4 Oxides

385 The oxides include Cr-spinel, titanomagnetite and ilmenite. We note that Cr-spinel and
386 titanomagnetite crystals do not contain internal Ti-rich exsolutions. Their compositions are
387 given in Table 6 and illustrated Figure 10. Cr-spinel crystals in the dunites and the wehrlites
388 of Sites 1 and 2 show overlapping compositions with high contents in Cr₂O₃ (26.32–45.24
389 wt%) and FeO_t (24.64–41.70 wt%), and moderate amounts of Al₂O₃ (8.77–17.77 wt%), MgO
390 (4.95–10.60 wt%) and TiO₂ (1.05–6.27 wt%). No Cr-spinel was observed at Sites 3 and 4,
391 and no titanomagnetite was observed at Sites 1 and 2. The titanomagnetite crystals at the Sites
392 3 and 4 show overlapping compositions, with contents at 2.89–26.35 wt% TiO₂, 1.49–9.81
393 wt% Al₂O₃, and 47.97–82.10 wt% FeO_t. Only two magnetite crystals were found in the study
394 area and only at Site 4: one at 88.65 wt% FeO_t in a wehrlite, and another at 80.17 wt% FeO_t
395 in an olivine gabbro. Their composition is distinct from the titanomagnetite crystals with
396 contents in TiO₂ and Al₂O₃ lower than 1 wt% (Fig. 10a). The ilmenite crystals were found in
397 all types of plutonic rocks of Sites 2, 3, and 4 except in the wehrlites. Their chemical
398 compositions are in the range 43.2–54.89 wt% TiO₂, 0.03–1.28 w% Al₂O₃, and 38.35–52.35
399 wt% FeO_t. It is important to note that their FeO_t content increases while their TiO₂ content
400 decreases from the dunites of Site 2 to the olivine gabbros, gabbros and ferrogabbros of Sites
401 3 and 4 (Fig. 10).

402

403 5.3 Whole-rock geochemistry

404 The whole-rock composition of samples is reported in Table 7 and plotted in Figure 11.
405 Consistent with our petrographic analysis, the plutonic rocks of Sites 1 and 2 show ultramafic
406 compositions with high MgO contents (32.96–42.58 wt%) and low SiO₂, CaO, and TiO₂
407 contents (36.11–39.92 wt%, 0.72–4.23 wt%, and 0.16–0.74 wt%, respectively; Fig. 11). This
408 contrasts with the differentiated compositions of plutonic rocks at Sites 3 and 4 with more
409 intermediate MgO, SiO₂, CaO, and TiO₂ contents (6.75–22.06, 39.98–48.31, 11.36–16.66
410 wt%, and 0.70–4.93 wt%, respectively). Related to their various modes and mineralogy, the
411 olivine gabbros, gabbros and ferrogabbros show distinct chemical compositions, which are
412 best observed in the SiO₂ vs. TiO₂ space (Fig. 11d). The olivine gabbros have intermediate
413 contents in SiO₂ and low contents in TiO₂ (43.52–46.04 wt% and 0.70–0.93 wt%,
414 respectively), the gabbros have high contents in SiO₂ and intermediate contents in TiO₂

(46.30–48.31 wt% and 0.74–1.51 wt%, respectively), and the ferrogabbros are defined by low contents in SiO₂ and high contents in TiO₂ (39.98–41.88 wt% and 3.14–4.93 wt%, respectively). The sample CB2260513 has been classified as a gabbro under the microscope, but since it has 18.18 wt% FeO in bulk composition, it should be classified as a ferrogabbro instead. The chemical composition of rocks samples collected at Site 3 tends to overlap with five of the samples from the SLZ1 drill hole and referenced K31 through K35 (gabbros at 46.5–50 wt% SiO₂; 6.08–9.96 wt% MgO; 10.81–12.65 wt% CaO; 2.01–2.75 wt% TiO₂; Chovelon, 1986; Demange et al., 1989). One sample of olivine gabbro (K42) from the drill hole shows an intermediate mafic composition at high MgO (27.7 wt%) and low SiO₂, CaO and TiO₂ contents (43.9 wt%, 7.29 wt%, and 0.35 wt%, respectively) between the Sites 1–2 and the Sites 3–4.

The trace element composition of samples is given in Figure 11e. The chondrite-normalized REE enrichment patterns of dunites and wehrlites from Sites 1 and 2 appear similar and follow a simple slope of depletion as the atomic number increases from La to Lu (i.e. from LREE to HREE), with no Eu anomaly except for one sample from Site 2 (CB1150914). It is important to note that this pattern is similar and remarkably parallel to that of the erupted products of Piton des Neiges during its basaltic and differentiated stages, despite the 2 to 30 times dilution of REE in peridotites. The enrichment patterns of olivine gabbros, gabbros, and ferrogabbros of Sites 3 and 4 are similar to that of the dunites and wehrlites of Sites 1 and 2, at the difference that they have a marked depletion in LREE and a clear positive Eu anomaly. These rocks show relatively high concentrations in Gd to Lu in comparison with the erupted products of Piton des Neiges, with dilution factors of only 1 to 4. The samples show also two trends in the Th vs. Sm space (Fig. 11f): variable enrichments in Th and low Sm contents for the peridotitic rocks at Sites 1–2, and low Th and high Sm contents for the gabbroic rocks at Sites 3–4.

6 Discussion

6.1 Peridotites and layered gabbros

Previous studies on the gabbroic mass outcropping at Site 4 have suggested that these rocks are remnants of an ancient magma body that supplied the volcanic activity of Piton des

Neiges (Upton and Wadsworth 1972; Chevallier and Vatin-Perignon 1982; Upton et al. 2000; Pronost 2001). The structural and textural characteristics of these rocks, have indicated a variety of magmatic processes, including fractional crystallization, crystal settling, convection, and slumps. Our investigations in the Mât River reported three new plutonic outcrops (Sites 1, 2, and 3, Fig. 1c), which, combined with Site 4, offers a unique opportunity to scrutinize *in situ* the frozen dynamics of magma flowing and cooling within the magmatic system of Piton des Neiges volcano.

6.1.1 Peridotitic units

Sites 1 and 2 host peridotitic lithologies (dunites and wehrlites, Figs 4 and 5) and are primitive in nature, having abundant Mg- and Cr-rich minerals (Fo_{81–89.5} olivine, clinopyroxene at Mg# = 69 – 90, and Cr-spinel at 26.32 – 45.24 wt% Cr₂O₃, (Figs 7, 8, 10 and 12), and high bulk MgO contents (32.96–42.58 wt%, Fig. 11). A first assumption is that all those rocks are imprints of the crystallization of high-temperature and high-MgO magmas. The primitive composition of the peridotites and the lack of any evidence of tectonic exhumation suggest that these magmas did not significantly differentiate in deep storage before their crystallization at shallow levels (≤ 2.5 km depth) in the volcanic edifice.

According to the olivine-augite Mg-Fe-exchange geothermometer of Loucks (1996), the re-equilibration of the peridotite layers would have happened in the range 1130–1165 \pm 6 °C (Tab. 8). The peridotites display adcumulate and heteradcumulate textures in which clinopyroxene was clearly the second silicate phase to precipitate after olivine (Fig. 5). REE patterns confirm our textural observations and reject the cumulative origin of the clinopyroxene (Fig. 11e-f). The adcumulate peridotites may be interpreted as the result of melt segregation, settling, and accumulation (Coats 1936; Tait and Jaupart 1996; Cawthorn 1996) or *in situ* crystallization on the magma reservoir margins (Campbell 1977; Walker et al. 1988; Marsh 1996).

The fact that the peridotites at Sites 1 and 2 have a similar enrichment pattern in REE with the erupted products of Piton des Neiges volcano (Fig. 11f-e) suggests that the two are related genetically. These outcrops represent the first tangible evidence of a primitive, consolidated magma body at Piton des Neiges volcano, which was inferred indirectly from gravimetric surveys (Malengreau et al. 1999; Gailler and Lénat 2012) and the presence of peridotitic xenoliths in the erupted products (Upton and Wadsworth 1972; Upton et al. 2000).

Finally, the fact that the peridotites are crosscut by thick anorthositic veinlets indicates a late transport of residual melts through the plutonic rocks after partial to complete solidification (Pallister and Hopson 1981). Given the geochemical similarity of the host rocks and veinlets, it is likely that these anorthositic melts result from local mineral and melt segregation (Figs 9 and 12).

6.1.2 Layered gabbros

The plutonic rocks outcropping at Sites 3 and 4 present more differentiated compositions, with gabbroic lithologies (wehrlites, olivine gabbros, gabbros, ferrogabbros and anorthosites, Figs 4 and 6), intermediate mineral compositions (Fo_{69-79} olivine, clinopyroxene at $\text{Mg\#} = 73 - 86$, An_{47-87} plagioclase, and FeTi-oxides, Figs 7–10 and 12), and moderate to low bulk MgO contents (6.75–22.06 wt%, Fig. 11). These outcrops provide evidence of crystallization from magmas having an intermediate composition. The estimated temperatures of re-equilibration from Loucks (1996) suggest that the gabbroic layers of Sites 3 and 4 were at about $1039 - 1118 \pm 6$ °C, i.e. at temperatures lower than the peridotites at Sites 1 and 2 (Tab. 8). The thin layering, the pronounced lineation, and the abundance of discontinuous and folded layering, syn magmatic faults, cross bedding and schlierens at Site 3 (Fig. 2d-f) suggest a high-energy environment (Wager and Brown 1967; McBirney and Noyes 1979; Hunter and Sparks 1987; Hoover 1989; McBirney and Nicolas 1997; Irvine et al. 1998; McBirney 2009). In contrast, the magmatic flow at Site 4 appears relatively more regular and laminar, with scarcer structures relatable to a high-energy environment (Fig. 2g-f). Any single or even a few cases of igneous layers can be successfully explained by one or a combination of several mechanisms (Cawthorn 1996). It is important to note that Berthod (2016) showed that the plutonic body occurring in the Mât River displays the same palaeomagnetic signature than La Montagne massif (Quidelleur et al. 2010) and consequently suggests that the plutonic rocks outcropping at Site 3 were not tectonically tilted from their since 2.2 Ma. Thus, because layering have not been moved from their original position and are strongly inclined ($43-44^\circ\text{S}$, Fig. 3), we suggest that the dynamic structures observed at Sites 3 and 4 were sorted and deposited by settling and magmatic crystal-liquid suspension currents, sometimes coupled with convective boundary-layer currents (Irvine et al. 1998). It is also likely that convective turbulences occurred in the reservoir through the influxes of fresh mafic magma into the chamber (Jaques 1981; Holness 2005).

We consider two different origins for these magmas: either they come from deeper levels in the edifice (following the classic model of shield building after Wolfe et al., 1997), or they come from the differentiation of primitive magmas at a similar level in the edifice. The fact that the gabbroic rocks at the Sites 3–4 show different enrichment patterns, with a relative depletion in LREE, may indicate either a different magma, a mixing between the magma at Site 1–2 and another one, or fractionation processes within the same source. In the latter case, the change in enrichment pattern can be explained by extensive fractionation and accumulation of clinopyroxene (which are abundant in the peridotitic lenses but even more in the gabbroic layers; Table 2) given that this mineral has a higher affinity for HREE than for LREE (Duncan et al. 1989; Blundy and Wood 1994; Johnson 1998; Norman et al. 2005; Peters et al. 2016; Barrat and Bachèlery 2019). We note that clinopyroxene accumulation is evidenced by whole-rock and mineral geochemistry (Figs 11b-d and 12c).

Similarly to the veinlets in the peridotite units, we interpret the anorthositic veinlets in the layered gabbros as residues of late liquids that crosscut the plutonic bodies after their partial to complete solidification (Pallister and Hopson 1981).

6.2 Pluton dynamics: single reservoir or stacked intrusions?

Gravimetric and magnetotelluric studies, as well as the SLZ1 borehole, indicate a large (pluri-kilometric in diameter) igneous body underlying the cirque of Salazie. The four outcrops described here are inferred to belong to this large plutonic complex. Nevertheless, our field investigations also show that the four distinct plutonic outcrops are separated from each other by sheet intrusions and breccia deposits (Fig. 1c), it is unclear whether these outcrops correspond to four different magma bodies or to subparts of larger structures.

Given their similar textures (Fig. 5) and mineral chemistry (Figs 7–12 and Tab. 9) and the proximity of the outcrops (Site 1 at 950–1200 m asl, Site 2 at 850–940 m asl, and only ~700 m apart, Fig. 1c), it is likely that the peridotitic units at Sites 1–2 belong to the same plutonic complex. Similarly, the gabbroic rocks at Sites 3–4 have close textures (Fig. 6), mineral chemistry (Figs 7–12 and Tab. 9), and dynamic structures (Fig. 2) and they are located in the same vicinity (Site 3 at 750–870 m asl, Site 4 at 660–750 m asl, and only ~200 m apart, Fig. 1c), which, taken together, suggest that these gabbroic rocks might be parts of a same plutonic complex.

The question then arises as whether these gabbroic and peridotitic units correspond to a single petrologically and geochemically zoned magma reservoir (e.g., Skaergaard; Wager and Deer 1939; Wager and Brown 1968; McBirney 1995; Tegner et al. 2009a; Salmonsén and Tegner 2013), or to a stack of several independent intrusions as for many other layered plutons (Glazner et al. 2004; Morgan et al. 2008; Michel et al. 2008; Grocott et al. 2009; Leuthold et al. 2012; Leuthold et al. 2014). In an attempt to answer that question, the essential features of each site are summarized and compared in Table 9.

The single reservoir hypothesis is supported by trends in the whole-rock geochemistry, showing a northward decrease in MgO and an increase in SiO₂, CaO, Na₂O, K₂O and Fe₂O₃ in the order Site 1 => Site 2 => Site 4 => Site 3 (Tabs 7 and 9, Fig. 11). Accordingly, the forsterite content in olivine, the Mg number in clinopyroxene and the oxides, and the anorthite content in plagioclase all tend to decrease from one site to another according to the same sequence (Figs 7–10). This would hence point to fractional crystallization as the main magmatic process in a unique magma reservoir, yielding to the compositional evolution of the magma from mafic at Sites 1–2, to intermediate at Sites 4–3 (Fig. 12). However, this sequence of differentiation may appear incomplete since there are notable gaps in whole-rock and phase compositions between the Sites 1–2 and the Sites 4–3 (Figs 7–12 and Tab. 9). One possibility for these gaps is the lack of exposed series in between these sites. The peridotitic series and the gabbroic series only outcrop 900 m apart in the Mât River (Fig. 1c), and it is hence possible that, in between, buried under the breccia, lies a third mass of plutonic rocks that connects the Sites 1–2 to the Sites 4–3. In this case, the buried series would contain the rest of the plutonic record, with layers transitioning in chemical composition and mineral assemblage from peridotitic to gabbroic lithologies.

However, the single reservoir interpretation is complicated by the fact that the peridotitic units of Sites 1–2 occur at higher altitudes than the gabbroic ones of Sites 4–3, since the most mafic layers are usually set at the base of magma chambers and more differentiated layers atop (Cawthorn and Walraven 1998; Cawthorn 2007; Tegner et al. 2009b; Salmonsén and Tegner 2013). This forces us to consider that the succession of Sites 1–2–4–3 is an inverse plutonic sequence, which would thus correspond to a roof of the magma chamber. Layered series are not always observed in the upper parts of mafic reservoirs, perhaps because they seldom form in these regions, or because their preservation is more subject to magma dynamics and weathering than the lower series (Jaupart and Tait 1995). However, the processes related to their formation have been described in the upper parts of several sills,

intrusions, and lava lakes (e. g. Simkin 1967; Brown and Wager 1968; Helz et al. 1989; Latypov et al. 2007). One obstacle to that hypothesis is the compact texture of peridotitic layers at Sites 1–2, which seem particularly difficult to achieve in a context of density inversion where the crystals lay atop the melt. But many crystals would be locally plated by laminar currents against the margins of the magma chamber (McBirney and Noyes 1979; Pallister and Hopson 1981; Irvine 1982; Nicolas et al. 2009), and even grow behind the solidification front, trapped within the viscous melt (Marsh 1996; Marsh 2006). In fact, these processes could be consistent with the presence of residual glass in between the crystals of some of the samples (Fig. 5g-h). Given that the melt concentrates incompatible elements such as Sm and Th, the presence of interstitial glass in the peridotites of Sites 1–2 could explain their high Sm and Th contents. In contrast, the glass-poor gabbros of Sites 4–3 shows variable and low Sm contents. Moreover, the adcumulate textures observed in several samples from Sites 1–2 could be also consistent with crystallization and maturation of olivine within a thermal gradient (Walker et al. 1988).

Given the difficulties in interpreting the Site 1–2–4–3 sequence as belonging to a single zoned magma reservoir, it seems more plausible to consider that the sequence observed at Sites 1–2–4–3 represents a stack of several independent intrusions. Contrasted chondrite-normalized REE enrichment patterns (Fig. 11e) and Sm/Th behaviors (Fig. 11f) between Sites 1–2 and Sites 4–3 support this second interpretation. Moreover, because the REE enrichment of a parental magma undergoing extensive fractionation of clinopyroxene should be lower than that of the daughter liquid, the layered gabbroic rocks cannot derive from peridotitic magmas. Furthermore, the layered gabbros and the peridotites outcrops are separated by magmatic intrusions and breccia deposits, which is consistent with these outcrops representing distinct magma bodies (Figs 1c and 13a). All these lines of evidence seem to indicate that the plutonic rocks outcropping at Sites 1, 2, 3, and 4 by the Mât River represent at least two different intrusions, one peridotitic (Sites 1–2) and another one gabbroic (Sites 4–3). In this respect, the plutonic rocks excavated at SLZ1 drillhole might belong to the second intrusion. In consequence, we suggest that the plutonic complex of Piton des Neiges is more likely made by incremental stacking of several independent magma intrusions, rather than by solidification of a single large magma reservoir. Separated magma intrusions are consistent with the inferred plumbing system of shield volcanoes in which magmas are stored in distinct, small ponding zones and/or sills (Lénat and Bachèlery 1990; Poland et al. 2009; Peltier et al. 2010; Montgomery-Brown et al. 2011; Baker and Amelung 2012; Di Muro et al. 2014) and

support the assumption that the feeding system of a volcano can be made of an array of sills and dykes grown incrementally by an amalgamation of new magmatic injections (Deniel et al. 1987; Annen and Sparks 2002; Glazner et al. 2004; Gudmundsson 2012; Annen et al. 2015; Blundy and Annen 2016; Karakas et al. 2017; Cashman et al. 2017; Sparks et al. 2019).

6.3 Stages of pluton growth in the evolution of Piton des Neiges

The original volcanic summit was ~3.5 km asl (Fig. 13b) and these plutonic rocks outcrop at 650 to 1000 m asl. This implies that the magma was stored at ~2.5 km below the surface. This depth is consistent with the physical model of Ryan (1987) in which magmas are preferentially stored at levels of neutral buoyancy, commonly corresponding to depths of 2 – 4 km below volcanic edifices (Ryan 1988; Fodor and Galar 1997; Albarède et al. 1997; Bureau et al. 1998; Battaglia et al. 2005; Scoates et al. 2008; Welsch et al. 2009; Peltier et al. 2009; Famin et al. 2009; Allibon et al. 2011; Lénat et al. 2012; Baker and Amelung 2012; Larrea et al. 2013). The Piton des Neiges volcano is situated ~7 km above the ocean floor, which inhibits direct transfer of magma from deep crustal levels to the summit zone (Pinel and Jaupart 2000) and favours shallow crustal storage.

However, the striking differences between Sites 1–2, and Sites 4–3, in terms of petrology, geochemistry and structure, raise the question of their relationship and their integration in the evolution of Piton des Neiges volcano.

Indeed, the gabbroic series of Sites 4–3 are clearly discordant with the formations of Piton des Neiges due to the development of a main detachment that cuts the plutonic body during the shield building stage of Piton des Neiges while the gabbroic rocks were at a temperature < 250°C (Famin and Michon, 2010; Famin et al., 2016). The gabbroic series also show a marked depletion in LREE that makes a genetic link between these plutonic rocks and the mafic and differentiated lavas of Piton des Neiges rather unlikely. Conversely, the clinopyroxene crystals of the layered gabbros have geochemical affinities with those found as phenocrysts in the ankaramites of the La Montagne massif (2.1 – 1.9 Ma), on the northern flank of Piton des Neiges (McDougall and Watkins 1973; Quidelleur et al. 2010). In addition, the series at Sites 4–3 have petrological and geochemical similarities with the plutonic rocks excavated by the SLZ1 drill hole in the cirque of Salazie (Fig. 1b). These comparisons suggest that the gabbroic plutonic intrusion extends north of the observed outcrops. The southward dip of the gabbro layers at Sites 4–3 corroborates this interpretation by suggesting

that the gabbro unit is bulged northward. Based on their study of depocenters, Lebas et al. (2018) concluded that the eruptive center of Piton des Neiges in its first construction phase (“Proto-Piton des Neiges”) was located several kilometers north of the more recent eruptive center corresponding to the actual summit. It is thus tempting to attribute the gabbroic part of the plutonic complex of Piton des Neiges to the La Montagne phase (Quidelleur et al. 2010; Salvany et al. 2012), associated with an eruptive center located in the cirque of Salazie (Fig. 13b, EC Proto-PdN).

The presence of a detachment zone overlain by a breccia unit made of basaltic lavas at the contact with the plutonic rocks of Site 4 suggests that the plutonic complex was at the root of a large flank destabilization (Famin and Michon 2010; Chaput et al. 2014a; Berthod et al. 2016). The discordant contact between the layered gabbro and the debris avalanche deposits shows that the flank collapse removed a large part of the plutonic complex (Berthod 2016; Berthod et al. 2016). The collapse occurred once the upper parts of the layered gabbros were already solidified (Famin et al. 2016). We thus propose that the lateral offset between the summit of Piton des Neiges to the south (Fig. 1) and the deep dense body underlying the cirque of Salazie results from this structural failure that led to a migration of the volcanic center to the south (EC PdN in Fig. 13b, Gailler and Lénat 2012). The presence of a deeper dense body underlying the cirque of Cilaos revealed by geophysical data (Gailler and Lénat 2012) supports this assumption.

The mineral and whole-rock compositions of the peridotites of Sites 1–2, positioned at the foot of the current summit of Piton des Neiges (Figs 1 and 13b), are consistent with both the crystallization of Mg-rich magmas and the eruption of basalts and olivine-rich basalts during the shield-building stage of Piton des Neiges (Fig. 11). Moreover, the sills of peridotites at the Site 2 show a northward gentle dip concordant with those of the sills related to the basaltic period of Piton des Neiges (Fig. 2c). Therefore, we tentatively interpret the peridotites of Sites 1–2 as part of the magmatic system of Piton des Neiges (Fig. 13b, EC PdN). The primitive mineral compositions of the peridotites of Sites 1–2 suggest that these rocks crystallized from poorly differentiated magmas similar to those observed along the NW rift zone between Piton des Neiges and Piton de la Fournaise (Boudoire et al. 2019).

Finally, a batch of more differentiated magma was then intruded after the cooling of the peridotites and layered gabbros, yielding the syenite plutonic mass (younger than 0.35 Ma

according to McDougall, 1971) inserted in between the Sites 3 and 4 during the Phase IV of the Piton des Neiges (Page 1994).

7 Conclusions

Our petrological study of the plutonic rocks outcropping at Sites 1, 2, 3, and 4 of the Mât River provides new insights on the magmatic system of Piton des Neiges volcano. The four outcrops consist of dunites and wehrlites overlying layered olivine gabbros, gabbros, and ferrogabbros. The dunite and wehrlite layers may correspond to the lower parts of a magma reservoir, formed by crystal separation from a primitive magma, settling and accumulation as evidenced by their adcumulate and heteradcumulate textures. In contrast, the olivine gabbro, gabbro and ferrogabbro layers define a zone formed from differentiated magmas in a high-energy environment, as evidenced by the presence of overturned folds, schlierens, and discontinuous layering. These plutonic outcrops have diverse structural, textural and compositional features, and are interpreted as remnants of at least two independent magma bodies: one peridotitic and the other gabbroic. These two systems were active at different periods of time. The differences in whole rock and phase compositions of layered gabbros and peridotites support this hypothesis. Hence, we propose that the four outcrops are parts of a pluri-kilometric composite plutonic complex, built by successive stacks of genetically unrelated magma intrusions over the entire lifetime of shield-building. Pluton growth began with gabbroic magmas emplaced from a volcano center located in the cirque of Salazie, and then shifted to more mafic magma compositions, emplaced from a southward volcano center corresponding roughly to the present-day Piton des Neiges summit.

ACKNOWLEDGMENTS

We thank Pierre Belle for his participation in the fieldwork and Genevieve Lebeau for preparing the thin sections. This work is a part of a Ph.D. fellowship sponsored by Fonds Social Européen and Région Réunion. We thank James Scoates, an anonymous reviewer, and Editor Kelly Russell for constructive criticism and help in improving the manuscript. Chemical analyses were funded by INSU-CNRS grants “Sill’nSlip” and “Runrise”. This is IPGP contribution 4163. This is Laboratory of Excellence ClerVolc contribution number 431.

REFERENCES

706 Albarède, F., Luais, B., Fitton, G., Semet, M., Kaminski, E., Upton, B.G.J., Bachélery, P.,
707 Cheminée, J.-L., 1997. The geochemical regimes of Piton de la Fournaise Volcano
708 (Réunion) during the last 530 000 years. *J. Petrol.* **38**, 171–201.
709 <https://doi.org/10.1093/petroj/38.2.171>

710 Allibon, J., Bussy, F., Lewin, É., Darbellay, B., 2011. The tectonically controlled
711 emplacement of a vertically sheeted gabbro-pyroxenite intrusion : Feeder-zone of
712 an ocean-island volcano (Fuerteventura , Canary Islands). *Tectonophysics* **500**,
713 78–97. <https://doi.org/10.1016/j.tecto.2010.01.011>

714 Annen, C., Blundy, J.D., Leuthold, J., Sparks, R.S.J., 2015. Construction and evolution of
715 igneous bodies: Towards an integrated perspective of crustal magmatism. *Lithos*
716 **230**, 206–221.

717 Annen, C., Sparks, R.S.J., 2002. Effects of repetitive emplacement of basaltic intrusions on
718 thermal evolution and melt generation in the crust. *Earth Planet. Sci. Lett.* **203**,
719 937–955.

720 Augé, T., Lerebour, P., Rançon, J.-P., 1989. The Grand Brûlé exploration drilling: New data
721 on the deep framework of the Piton de la Fournaise volcano. Part 3: Mineral
722 chemistry of the cumulate rocks. *J. Volcanol. Geotherm. Res.* **36**, 139–151.
723 [https://doi.org/10.1016/0377-0273\(89\)90010-3](https://doi.org/10.1016/0377-0273(89)90010-3)

724 Baker, S., Amelung, F., 2012. Top-down inflation and deflation at the summit of Kilauea
725 Volcano, Hawaii observed with InSAR. *J. Geophys. Res. Solid Earth* **117**, 1–14.
726 <https://doi.org/10.1029/2011JB009123>

727 Barrat, J.-A., Bachélery, P., 2019. La Réunion Island dunites as analogs of the Martian
728 chassignites: Tracking trapped melts with incompatible trace elements. *Lithos* **344**,
729 452–463. <https://doi.org/10.1016/j.lithos.2019.07.009>

730 Battaglia, J., Aki, K., Staudacher, T., 2005. Location of tremor sources and estimation of
731 lava output using tremor source amplitude on the Piton de la Fournaise volcano: 2.
732 Estimation of lava output. *J. Volcanol. Geotherm. Res.* **147**, 291–308.
733 <https://doi.org/10.1016/j.jvolgeores.2005.04.006>

734 Berthod, C., 2016. Relation entre système intrusif et instabilités sur un volcan basaltique
735 (Piton des Neiges, La Réunion). Université de La Réunion.

736 Berthod, C., Famin, V., Bascou, J., Michon, L., Ildefonse, B., Monié, P., 2016. Evidence of
737 sheared sills related to flank destabilization in a basaltic volcano. *Tectonophysics*
738 **674**, 195–209. <http://dx.doi.org/10.1016/j.tecto.2016.02.017>

Blundy, J., Wood, B., 1994. Prediction of crystal–melt partition coefficients from elastic moduli. *Nature* **372**, 452. <https://doi.org/10.1038/372452a0>

Blundy, J.D., Annen, C.J., 2016. Crustal magmatic systems from the perspective of heat transfer. *Elements* **12**, 115–120.

Boudoire, G., Brugier, Y.-A., Di Muro, A., Wörner, G., Arienzo, I., Metrich, N., Zanon, V., Braukmüller, N., Kronz, A., Le Moigne, Y., 2019. Eruptive activity on the western flank of Piton de la Fournaise (La Réunion Island, Indian Ocean): insights on magma transfer, storage and evolution at an oceanic volcanic island. *J. Petrol.* **60**, 1717–1752.

Brown, G.M., Wager, L.R., 1968. Layered igneous rocks.

Bureau, H., Pineau, F., Métrich, N., Semet, M.P., Javoy, M., 1998. A melt and fluid inclusion study of the gas phase at Piton de la Fournaise volcano (Réunion Island). *Chem. Geol.* **147**, 115–130. [https://doi.org/10.1016/S0009-2541\(97\)00176-9](https://doi.org/10.1016/S0009-2541(97)00176-9)

Campbell, I.H., 1977. A study of macro-rhythmic layering and cumulate processes in the jamberlana intrusion, Western Australia. part I: The upper layered series. *J. Petrol.* **18**, 183–215. <https://doi.org/10.1093/petrology/18.2.183>

Cashman, K. V., Sparks, R.S.J., Blundy, J.D., 2017. Vertically extensive and unstable magmatic systems: a unified view of igneous processes. *Science*. **355**, eaag3055.

Cawthorn, R., Walraven, F., 1998. Emplacement and crystallization time for the Bushveld Complex. *J. Petrol.* **39**, 1669–1687. <https://doi.org/10.1093/petrology/39.9.1669>

Cawthorn, R.G., 2007. Cr and Sr: Keys to parental magmas and processes in the Bushveld Complex, South Africa. *Lithos* **95**, 381–398. <https://doi.org/10.1016/j.lithos.2006.09.004>

Cawthorn, R.G., 1996. Layered intrusions. Elsevier.

Chaput, M., Famin, V., Michon, L., 2014a. Deformation of basaltic shield volcanoes under cointrusive stress permutations. *J. Geophys. Res. Solid Earth* **119**, 274–301. <https://doi.org/10.1002/2013jb010623>

Chaput, M., Pinel, V., Famin, V., Michon, L., Froger, J.-L., 2014b. Cointrusive shear displacement by sill intrusion in a detachment: A numerical approach. *Geophys. Res. Lett.* **41**, 799–804. <https://doi.org/10.1002/2013GL058813>

Chevallier, L., Vatin-Perignon, N., 1982. Volcano-structural evolution of Piton des Neiges, Reunion Island, Indian Ocean. *Bull. Volcanol.* **45**, 285–298. <https://doi.org/10.1007/BF02597253>

772 Chovelon, P., 1986. Forage géothermique de Salazie SLZI, Etude géologique du forage.
 773 Rapport 86CFG018.

774 Coats, R.R., 1936. Primary banding in basic plutonic rocks. *J. Geol.* **44**, 407–419.

775 Courtillot, V., Davaille, A., Besse, J., Stock, J., 2003. Three distinct types of hotspots in the
 776 Earth's mantle. *Earth Planet. Sci. Lett.* **205**, 295–308.
 777 [https://doi.org/10.1016/S0012-821X\(02\)01048-8](https://doi.org/10.1016/S0012-821X(02)01048-8)

778 de Voogd, B., Pou Palomé, S., Hirn, A., Charvis, P., Gallart, J., Rousset, D., Danobeitia, J.,
 779 Perroud, H., 1999. Vertical movements and material transport during hotspot
 780 activity: Seismic reflection profiling offshore La Réunion. *Geophys. Res. Lett.* **104**,
 781 2855–2874. <https://doi.org/10.1029/98JB02842>

782 Demange, J., Chovelon, P., Puvilland, P., 1989. Geothermal model of the Salazie Cirque
 783 (Reunion Island) : Volcanic and structural implications. *J. Volcanol. Geotherm. Res.*
 784 **36**, 153–176. [https://doi.org/10.1016/0377-0273\(89\)90011-5](https://doi.org/10.1016/0377-0273(89)90011-5)

785 Deniel, C., Vidal, P., Fernandez, A., Le Fort, P., Peucat, J.-J., 1987. Isotopic study of the
 786 Manaslu granite (Himalaya, Nepal): inferences on the age and source of Himalayan
 787 leucogranites. *Contrib. to Mineral. Petrol.* **96**, 78–92.

788 Di Muro, A., Métrich, N., Vergani, D., Rosi, M., Armienti, P., Fougereux, T., Deloule, E.,
 789 Arienzo, I., Civetta, L., 2014. The shallow plumbing system of Piton de la Fournaise
 790 Volcano (La Reunion Island, Indian Ocean) revealed by the major 2007 caldera-
 791 forming eruption. *J. Petrol.* **55**, 1287–1315.
 792 <https://doi.org/10.1093/petrology/egu025>

793 Duncan, R.A., Backman, J., Peterson, L., Party, T.S.S., 1989. Reunion hotspot activity
 794 through tertiary time: Initial results from the ocean drilling program, leg 115. *J.*
 795 *Volcanol. Geotherm. Res.* **36**, 193–198. [https://doi.org/10.1016/0377-](https://doi.org/10.1016/0377-0273(89)90013-9)
 796 [0273\(89\)90013-9](https://doi.org/10.1016/0377-0273(89)90013-9)

797 Edmonds, M., Cashman, K. V, Holness, M., Jackson, M., 2019. Architecture and dynamics
 798 of magma reservoirs *A* **377**: 20180298. <https://doi.org/10.1098/rsta.2018.0298>

799 Famin, V., Berthod, C., Michon, L., Eychenne, J., Brothelande, E., Mahabot, M.-M., Chaput,
 800 M., 2016. Localization of magma injections, hydrothermal alteration, and
 801 deformation in a volcanic detachment (Piton des Neiges, La Réunion). *J. Geodyn.*
 802 **101**, 155–169. <https://doi.org/https://doi.org/10.1016/j.jog.2016.05.007>

803 Famin, V., Michon, L., 2010. Volcano destabilization by magma injections in a
 804 detachment. *Geology* **38**, 219–222. <https://doi.org/10.1130/G30717.1>

805 Famin, V., Welsch, B., Okumura, S., Bachèlery, P., Nakashima, S., 2009. Three
806 differentiation stages of a single magma at Piton de la Fournaise volcano (Reunion
807 hot spot). *Geochemistry, Geophys. Geosystems* **10**, 1–18.
808 <https://doi.org/10.1029/2008GC002015>

809 Fisk, M.R., Upton, B.G.J., Ford, C.E., White, W.M., 1988. Geochemical and experimental
810 study of the genesis of magmas of Réunion Island, Indian Ocean. *J. Geophys. Res.* **93**,
811 4933–4950. <https://doi.org/10.1029/JB093iB05p04933>

812 Fodor, R. V, Galar, P., 1997. A view into the subsurface of Mauna Kea volcano, Hawaii:
813 crystallization processes interpreted through the petrology and petrography of
814 gabbroic and ultramafic xenoliths. *J. Petrol.* **38**, 581–624.
815 <https://doi.org/10.1093/petroj/38.5.581>

816 Gailler, L.-S., Lénat, J.-F., Lambert, M., Levieux, G., Villeneuve, N., Froger, J.-L., 2009.
817 Gravity structure of Piton de la Fournaise volcano and inferred mass transfer
818 during the 2007 crisis. *J. Volcanol. Geotherm. Res.* **184**, 31–48.
819 <https://doi.org/10.1016/j.jvolgeores.2009.01.024>

820 Gailler, L., 2010. Structure interne d'un système volcanique océanique de type point
821 chaud: La Réunion (Océan Indien)-Approches géophysiques.

822 Gailler, L.S., Lénat, J.F., 2012. Internal architecture of La Réunion (Indian Ocean) inferred
823 from geophysical data. *J. Volcanol. Geotherm. Res.* **221–222**, 83–98.
824 <https://doi.org/10.1016/j.jvolgeores.2012.01.015>

825 Gailler, L.S., Lénat, J.F., 2010. Three-dimensional structure of the submarine flanks of La
826 Réunion inferred from geophysical data. *J. Geophys. Res. Solid Earth* **115**, 1–27.
827 <https://doi.org/10.1029/2009JB007193>

828 Gayer, E., Michon, L., Louvat, P., Gaillardet, J., 2019. Storm-induced precipitation
829 variability control of long-term erosion. *Earth Planet. Sci. Lett.* **517**, 61–70.
830 <https://doi.org/10.1016/j.epsl.2019.04.003>

831 Gillot, P.-Y., Lefèvre, J.-C., Nativel, P.-E., 1994. Model for the structural evolution of the
832 volcanoes of Réunion Island. *Earth Planet. Sci. Lett.* **122**, 291–302.
833 [https://doi.org/10.1016/0012-821X\(94\)90003-5](https://doi.org/10.1016/0012-821X(94)90003-5)

834 Gillot, P.-Y., Nativel, P., 1982. K/Ar chronology of the ultimate activity of Piton des Neiges
835 volcano, Reunion Island, Indian Ocean. *J. Volcanol. Geotherm. Res.* **13**, 131–146.
836 [https://doi.org/https://doi.org/10.1016/0377-0273\(82\)90024-5](https://doi.org/https://doi.org/10.1016/0377-0273(82)90024-5)

837 Glazner, A.F., Bartley, J.M., Coleman, D.S., Gray, W., Taylor, R.Z., 2004. Are plutons

838 assembled over millions of years by amalgamation from small magma chambers?
839 GSA today **14**, 4–12.

840 Grocott, J., Arévalo, C., Welkner, D., Cruden, A., 2009. Fault-assisted vertical pluton
841 growth: Coastal Cordillera, north Chilean Andes. *J. Geol. Soc. London.* **166**, 295–301.

842 Gudmundsson, A., 2012. Magma chambers : Formation , local stresses , excess pressures
843 , and compartments. *J. Volcanol. Geotherm. Res.* **237–238**, 19–41.
844 <https://doi.org/10.1016/j.jvolgeores.2012.05.015>

845 Helz, R.T., Kirschenbaum, H., Marinenko, J.W., 1989. Diapiric transfer of melt in Kilauea
846 Iki lava lake, Hawaii: a quick, efficient process of igneous differentiation. *Geol. Soc.
847 Am. Bull.* **101**, 578–594.

848 Holness, M.B., 2005. Spatial constraints on magma chamber replenishment events from
849 textural observations of cumulates: The Rum Layered Intrusion, Scotland. *J. Petrol.*
850 **46**, 1585–1601. <https://doi.org/10.1093/petrology/egi027>

851 Hoover, J.D., 1989. Petrology of the marginal border series of the skaergaard intrusion. *J.*
852 *Petrol.* **30**, 399–439. <https://doi.org/10.1093/petrology/30.2.399>

853 Hunter, R.H., Sparks, R.S.J., 1987. The differentiation of the Skaergaard Intrusion.
854 *Contrib. to Mineral. Petrol.* **95**, 451–461. <https://doi.org/10.1007/BF00402205>

855 Irvine, T.N., 1982. Terminology for layered intrusions. *J. Petrol.* **23**, 127–162.

856 Irvine, T.N., Andersen, J.C.Ø., Brooks, C.K., 1998. Included blocks (and blocks within
857 blocks) in the Skaergaard intrusion: Geologic relations and the origins of rhythmic
858 modally graded layers. *Bull. Geol. Soc. Am.* **110**, 1398–1447.
859 [https://doi.org/10.1130/0016-7606\(1998\)110<1398:IBABWB>2.3.CO;2](https://doi.org/10.1130/0016-7606(1998)110<1398:IBABWB>2.3.CO;2)

860 Jackson, M.D., Blundy, J., Sparks, R.S.J., 2018. Chemical differentiation, cold storage and
861 remobilization of magma in the Earth’s crust. *Nature* **564**, 405–409.

862 Jaques, A.L., 1981. Petrology and petrogenesis of cumulate peridotites and gabbros from
863 the marum ophiolite complex, Northern Papua New Guinea. *J. Petrol.* **22**, 1–40.
864 <https://doi.org/10.1093/petrology/22.1.1>

865 Jaupart, C., Tait, S., 1995. Dynamics of differentiation in magma reservoirs. *J. Geophys.*
866 *Res. Solid Earth* **100**, 17615–17636.

867 Johnson, K.T.M., 1998. Experimental determination of partition coefficients for rare
868 earth and high-field-strength elements between clinopyroxene, garnet, and basaltic
869 melt at high pressures. *Contrib. to Mineral. Petrol.* **133**, 60–68.
870 <https://doi.org/10.1007/s004100050437>

871 Karakas, O., Degruyter, W., Bachmann, O., Dufek, J., 2017. Lifetime and size of shallow
872 magma bodies controlled by crustal-scale magmatism. *Nat. Geosci.* **10**, 446–450.

873 Kluska, J.M., 1997. Evolution magmatique et morpho-structurale du Piton des Neiges au
874 cours des derniers 500 000 ans. Université Paris XI - Orsay.

875 Lacroix, A., 1936. Le Volcan actif de l'île de la Réunion et ses produits.[-Le volcan actif de
876 l'île de la Réunion (supplément) et celui de la Grande-Comore]. Gauthier-Villars.

877 Lacroix, A., 1923. Minéralogie de Madagascar. A. Challamel, éditeur, Librairie maritime
878 et coloniale.

879 Lacroix, A., 1916. Sur quelques roches volcaniques mélanocrates des Possessions
880 françaises de l'océan Indien et du Pacifique. *Comptes Rendus* **163**, 182–183.

881 Larrea, P., França, Z., Lago, M., Widom, E., Galé, C., Ubide, T., 2013. Magmatic Processes
882 and the Role of Antecrysts in the Genesis of Corvo Island (Azores Archipelago ,
883 Portugal). *J. Petrol.* **54**, 769–793. <https://doi.org/10.1093/petrology/egs084>

884 Latypov, R., Chistyakova, S., Alapieti, T., 2007. Revisiting problem of chilled margins
885 associated with marginal reversals in mafic-ultramafic intrusive bodies. *Lithos* **99**,
886 178–206. <https://doi.org/10.1016/j.lithos.2007.05.008>

887 Le Friant, A., Lebas, E., Clément, V., Boudon, G., Deplus, C., De Voogd, B., Bachelery, P.,
888 2011. A new model for the evolution of la Réunion volcanic complex from complete
889 marine geophysical surveys. *Geophys. Res. Lett.* **38**, 6–11.
890 <https://doi.org/10.1029/2011GL047489>

891 Lebas, E., Le Friant, A., Deplus, C., de Voogd, B., 2018. Understanding the Evolution of an
892 Oceanic Intraplate Volcano From Seismic Reflection Data: A New Model for La
893 Réunion, Indian Ocean. *J. Geophys. Res. Solid Earth* **123**, 1035–1059.
894 <https://doi.org/10.1002/2017JB014959>

895 Lénat, J., Gibert-Malengreau, B., Galdéano, A., 2001. A new model for the evolution of the
896 volcanic island of Reunion (Indian Ocean). *J. Geophys. Res. Solid Earth* **106**, 8645–
897 8663. <https://doi.org/10.1029/2000JB900448>

898 Lénat, J.F., Bachelery, P., 1990. Structure and dynamics of the central zone of Piton de la
899 Fournaise volcano. *Le Volcanisme la Réunion*. Lénat, J.-F.(Ed.), *Le volcanisme la*
900 *Réunion—Monographie Cent. Rech. en Volcanol.* Clermont-Ferrand, Fr. 257–296.

901 Lénat, J.F., Bachelery, P., Peltier, A., 2012. The interplay between collapse structures,
902 hydrothermal systems, and magma intrusions: The case of the central area of Piton
903 de la Fournaise volcano. *Bull. Volcanol.* **74**, 407–421.

<https://doi.org/10.1007/s00445-011-0535-3>
 Lerebour, P., Rançon, J.P., Augé, T., 1989. The Grand Brûlé exploration drilling: new data on the deep framework of the Piton de la Fournaise volcano. Part 2: secondary minerals. *J. Volcanol. Geotherm. Res.* **36**, 129–137.
 Leuthold, J., Müntener, O., Baumgartner, L.P., Putlitz, B., 2014. Petrological constraints on the recycling of mafic crystal mushes and intrusion of braided sills in the Torres del Paine mafic complex (Patagonia). *J. Petrol.* **55**, 917–949.
 Leuthold, J., Müntener, O., Baumgartner, L.P., Putlitz, B., Ovtcharova, M., Schaltegger, U., 2012. Time resolved construction of a bimodal laccolith (Torres del Paine, Patagonia). *Earth Planet. Sci. Lett.* **325**, 85–92.
 Loucks, R.R., 1996. A precise olivine-augite Mg-Fe-exchange geothermometer. *Contr. Min. Pet.* **125**, 140. <https://doi.org/10.1007/s004100050211>
 Mahoney, J.J., Duncan, R.A., Khan, W., Gnos, E., McCormick, G.R., 2002. Cretaceous volcanic rocks of the South Tethyan suture zone, Pakistan: implications for the Réunion hotspot and Deccan Traps. *Earth Planet. Sci. Lett.* **203**, 295–310. [https://doi.org/10.1016/S0012-821X\(02\)00840-3](https://doi.org/10.1016/S0012-821X(02)00840-3)
 Malengreau, B., Lénat, J.-F., Froger, J.-L., 1999. Structure of Réunion Island (Indian Ocean) inferred from the interpretation of gravity anomalies. *J. Volcanol. Geotherm. Res.* **88**, 131–146. [https://doi.org/10.1016/S0377-0273\(98\)00114-0](https://doi.org/10.1016/S0377-0273(98)00114-0)
 Marsh, B.D., 2006. Dynamics of magmatic systems. *Elements* **2**, 287–292.
 Marsh, B.D., 1996. Solidification fronts and magmatic evolution. *Mineral. Mag.* **60**, 5–40. <https://doi.org/10.1180/minmag.1996.060.398.03>
 McBirney, a. R., 1995. Mechanisms of differentiation in the Skaergaard Intrusion. *J. Geol. Soc. London.* **152**, 421–435. <https://doi.org/10.1144/gsjgs.152.3.0421>
 McBirney, A.R., 2009. Factors governing the textural development of Skaergaard gabbros: A review. *Lithos* **111**, 1–5. <https://doi.org/10.1016/j.lithos.2008.09.009>
 McBirney, A.R., Nicolas, A., 1997. The Skaergaard Layered Series. Part II. Magmatic flow and Dynamic Layering. *J. Petrol.* **38**, 569–580. <https://doi.org/10.1093/petroj/38.5.569>
 McBirney, A.R., Noyes, R.M., 1979. Crystallization and layering of the skaergaard intrusion. *J. Petrol.* **20**, 487–554. <https://doi.org/10.1093/petrology/20.3.487>
 McDonough, W.F., Sun, S.-S., 1995. The composition of the Earth. *Chem. Geol.* **120**, 223–253. [https://doi.org/10.1016/0009-2541\(94\)00140-4](https://doi.org/10.1016/0009-2541(94)00140-4)

937 McDougall, I., 1971. The geochronology and evolution of the young volcanic island of
 938 Réunion, Indian Ocean. *Geochim. Cosmochim. Acta* **35**, 261–288.
 939 [https://doi.org/10.1016/0016-7037\(71\)90037-8](https://doi.org/10.1016/0016-7037(71)90037-8)
 940 Michel, J., Baumgartner, L., Putlitz, B., Schaltegger, U., Ovtcharova, M., 2008. Incremental
 941 growth of the Patagonian Torres del Paine laccolith over 90 ky. *Geology* **36**, 459–
 942 462.
 943 Montgomery-Brown, E.K., Sinnett, D.K., Larson, K.M., Poland, M.P., Segall, P., Miklius, A.,
 944 2011. Spatiotemporal evolution of dike opening and decollement slip at Kilauea
 945 Volcano, Hawaii. *J. Geophys. Res. Solid Earth* **116**, 1–14.
 946 <https://doi.org/10.1029/2010JB007762>
 947 Morgan, S., Stanik, A., Horsman, E., Tikoff, B., de Saint Blanquat, M., Habert, G., 2008.
 948 Emplacement of multiple magma sheets and wall rock deformation: Trachyte Mesa
 949 intrusion, Henry Mountains, Utah. *J. Struct. Geol.* **30**, 491–512.
 950 <https://doi.org/10.1016/j.jsg.2008.01.005>
 951 Nativel, P., 1978. Volcans de La Réunion: pétrologie, facies zéolite (Piton des Neiges)
 952 sublimes (Piton de la Fournaise). Orsay.
 953 Nicolas, A., Boudier, F., France, L., 2009. Subsidence in magma chamber and the
 954 development of magmatic foliation in Oman ophiolite gabbros. *Earth Planet. Sci.*
 955 *Lett.* **284**, 76–87. <https://doi.org/10.1016/j.epsl.2009.04.012>
 956 Norman, M., Garcia, M.O., Pietruszka, A.J., 2005. Trace-element distribution coefficients
 957 for pyroxenes, plagioclase, and olivine in evolved tholeiites from the 1955 eruption
 958 of Kilauea Volcano, Hawai'i, and petrogenesis of differentiated rift-zone lavas. *Am.*
 959 *Mineral.* **90**, 888–899. <https://doi.org/10.2138/am.2005.1780>
 960 Oversby, V.M., 1972. Genetic relations among the volcanic rocks of Reunion: chemical
 961 and lead isotopic evidence. *Geochim. Cosmochim. Acta* **36**, 1167–1179.
 962 [https://doi.org/10.1016/0016-7037\(72\)90097-X](https://doi.org/10.1016/0016-7037(72)90097-X)
 963 Page, B.A., 1994. Late-stage evolution of Piton des Neiges volcano, La Réunion.
 964 Pallister, J.S., Hopson, C. a., 1981. Samail Ophiolite plutonic suite: Field relations, phase
 965 variation, cryptic variation and layering, and a model of a spreading ridge magma
 966 chamber. *J. Geophys. Res.* **86**, 2593. <https://doi.org/10.1029/JB086iB04p02593>
 967 Peltier, A., Bachèlery, P., Staudacher, T., 2009. Magma transport and storage at Piton de
 968 La Fournaise (La Réunion) between 1972 and 2007: A review of geophysical and
 969 geochemical data. *J. Volcanol. Geotherm. Res.* **184**, 93–108.

970 <https://doi.org/10.1016/j.jvolgeores.2008.12.008>

971 Peltier, A., Staudacher, T., Bachèlery, P., 2010. New behaviour of the Piton de La
 972 Fournaise volcano feeding system (La Réunion Island) deduced from GPS data:
 973 Influence of the 2007 Dolomieu caldera collapse. *J. Volcanol. Geotherm. Res.* **192**,
 974 48–56. <https://doi.org/10.1016/j.jvolgeores.2010.02.007>

975 Peters, B.J., Day, J.M.D., Taylor, L.A., 2016. Early mantle heterogeneities in the Réunion
 976 hotspot source inferred from highly siderophile elements in cumulate xenoliths.
 977 *Earth Planet. Sci. Lett.* **448**, 150–160. <https://doi.org/10.1016/j.epsl.2016.05.015>

978 Pinel, V., Jaupart, C., 2000. The effect of edifice load on magma ascent beneath a volcano.
 979 *Philos. Trans. R. Soc. London A Math. Phys. Eng. Sci.* **358**, 1515–1532.
 980 <https://doi.org/10.1098/rsta.2000.0601>

981 Poland, M.P., Jeff Sutton, A., Gerlach, T.M., 2009. Magma degassing triggered by static
 982 decompression at Kilauea Volcano, Hawai'i. *Geophys. Res. Lett.* **36**, 1–5.
 983 <https://doi.org/10.1029/2009GL039214>

984 Pronost, J., 2001. Etudes des relations entre réservoirs magmatiques: un exemple à l'île
 985 de La Réunion.

986 Quidelleur, X., Holt, J.W., Salvany, T., Bouquerel, H., 2010. New K-Ar ages from La
 987 Montagne massif, Réunion Island (Indian Ocean), supporting two geomagnetic
 988 events in the time period 2.2–2.0 Ma. *Geophys. J. Int.* **182**, 699–710.
 989 <https://doi.org/10.1111/j.1365-246X.2010.04651.x>

990 Rançon, J.P., Lerebour, P., Augé, T., 1989. The Grand Brule exploration drilling: New data
 991 on the deep framework of the Piton de la Fournaise volcano. Part 1:
 992 Lithostratigraphic units and volcanostructural implications. *J. Volcanol. Geotherm.*
 993 *Res.* **36**, 113–127. [https://doi.org/10.1016/0377-0273\(89\)90008-5](https://doi.org/10.1016/0377-0273(89)90008-5)

994 Rousset, D., Lesquer, A., Bonneville, A., Lénat, J.F., 1989. Complete gravity study of Piton
 995 de la Fournaise volcano, Réunion Island. *J. Volcanol. Geotherm. Res.* **36**, 37–52.
 996 [https://doi.org/10.1016/0377-0273\(89\)90004-8](https://doi.org/10.1016/0377-0273(89)90004-8)

997 Ryan, M., 1988. The mechanics and three-dimensional internal structure of active
 998 magmatic systems: Kilauea volcano, Hawaii. *J. Geophys. Res.* **93**, 4213–4248.
 999 <https://doi.org/10.1029/JB093iB05p04213>

1000 Ryan, M.P., 1987. Neutral buoyancy and the mechanical evolution of magmatic systems.
 1001 No. 1. University Park, Pa.: The Geochemical Society, in: *Geochem. Soc. University*
 1002 *Park, P. (Ed.), Magmatic Processes: Physicochemical Principles; Special Publication.*

1003 pp. 259–287.

1004 Salmonsén, L.P., Tegner, C., 2013. Crystallization sequence of the Upper Border Series of
 1005 the Skaergaard Intrusion: Revised subdivision and implications for chamber-scale
 1006 magma homogeneity. *Contrib. to Mineral. Petrol.* **165**, 1155–1171.
 1007 <https://doi.org/10.1007/s00410-013-0852-y>

1008 Salvany, T., Lahitte, P., Nativel, P., Gillot, P.Y., 2012. Geomorphic evolution of the Piton
 1009 des Neiges volcano (Réunion Island, Indian Ocean): Competition between volcanic
 1010 construction and erosion since 1.4Ma. *Geomorphology* **136**, 132–147.
 1011 <https://doi.org/10.1016/j.geomorph.2011.06.009>

1012 Scoates, J.S., Weis, D., Franssens, M., Mattielli, N., Annell, H., Frey, F.A., Nicolaysen, K.,
 1013 Giret, A., 2008. The Val Gabbro Plutonic Suite : A Sub-volcanic Intrusion Emplaced
 1014 at the End of Flood Basalt Volcanism on the Kerguelen Archipelago. *J. Petrol.* **49**,
 1015 79–105. <https://doi.org/10.1093/petrology/egm071>

1016 Simkin, T., 1967. Flow differentiation in the picritic sills of North Skye. *Ultramafic Relat.*
 1017 *rocks* 64–70.

1018 Smietana, M., 2011. *Pétrologie, géochronologie (K–Ar) et géochimie élémentaire et*
 1019 *isotopique (Sr, Nd, Hf, Pb) des laves anciennes de La Réunion. Implications sur la*
 1020 *construction de l'édifice volcanique. Université de La Réunion.*

1021 Sobolev, A. V, Nikogosian, I.K., 1994. Petrology of long-lived mantle plume magmatism:
 1022 Hawaii, Pacific and Reunion Island, Indian Ocean. *Petrology* **2**, 111–144.

1023 Sparks, R.S.J., Annen, C., Blundy, J.D., Cashman, K. V, Rust, A.C., Jackson, M.D., 2019.
 1024 Formation and dynamics of magma reservoirs. *Philos. Trans. R. Soc. A* **377**,
 1025 20180019.

1026 Szymanowski, D., Wotzlaw, J.-F., Ellis, B.S., Bachmann, O., Guillong, M., von Quadt, A.,
 1027 2017. Protracted near-solidus storage and pre-eruptive rejuvenation of large
 1028 magma reservoirs. *Nat. Geosci.* **10**, 777–782.

1029 Tait, S.R., Jaupart, C., 1996. The production of chemically stratified and adcumulate
 1030 plutonic igneous rocks. *Mineral. Mag.* **60**, 99–114.
 1031 <https://doi.org/10.1180/minmag.1996.060.398.07>

1032 Tegner, C., Peter, T., Holness, M.B., Jakobsen, J.K., Leshner, C.E., 2009a. Differentiation and
 1033 compaction in the Skaergaard intrusion. *J. Petrol.* **50**, 813–840.
 1034 <https://doi.org/10.1093/petrology/egp020>

1035 Tegner, C., Thy, P., Holness, M.B., Jakobsen, J.K., Leshner, C.E., 2009b. Differentiation and

1036 compaction in the Skaergaard intrusion. *J. Petrol.* **50**, 813–840.
 1037 <https://doi.org/10.1093/petrology/egp020>

1038 Tornare, E., Pilet, S., Bussy, F., 2016. Magma Differentiation in Vertical Conduits Revealed
 1039 by the Complementary Study of Plutonic and Volcanic Rocks from Fuerteventura
 1040 (Canary Islands). *J. Petrol.* **57**, 2221–2250.
 1041 <https://doi.org/10.1093/petrology/egx004>

1042 Upton, B.G.J., Semet, M.P., Joron, J.L., 2000. Cumulate clasts in the Bellecombe Ash
 1043 Member, Piton de la Fournaise, Réunion Island, and their bearing on cumulative
 1044 processes in the petrogenesis of the Réunion lavas. *J. Volcanol. Geotherm. Res.* **104**,
 1045 297–318. [https://doi.org/10.1016/S0377-0273\(00\)00212-2](https://doi.org/10.1016/S0377-0273(00)00212-2)

1046 Upton, B.G.J., Wadsworth, W.J., 1972. Peridotite and gabbroic rocks associated with
 1047 shield-forming lavas of Réunion. *Contrib. to Mineral. Petrol.* **35**, 139–158.
 1048 <https://doi.org/10.1007/BF00370925>

1049 Upton, B.G.J., Wadsworth, W.J., 1967. A complex basalt-mugearite sill in Piton des Neiges
 1050 volcano, Réunion. *Am. Mineral.* **52**, 1475–1492.

1051 Upton, B.G.J., Wadsworth, W.J., 1966. The basalts of Reunion Island, Indian Ocean. *Bull.*
 1052 *Volcanol.* **29**, 7–23. <https://doi.org/10.1007/BF02597136>

1053 Vincent, B. de Saint, 1804. Voyage dans les quatre principales îles des mers d’Afrique.

1054 Wager, L.R., Brown, G.M., 1968. General features of the Skaregaard intrusion.

1055 Wager, L.R., Brown, G.M., 1967. Layered igneous rocks.

1056 Wager, L.R., Deer, W.A., 1939. Geological investigations in East Greenland, pt. 3, The
 1057 petrology of the Skaergaard intrusion, Kangerdlugssuaq, East Greenland.

1058 Walker, D., Jurewicz, S., Watson, E.B., 1988. Adcumulus dunite growth in a laboratory
 1059 thermal gradient. *Contrib. to Mineral. Petrol.* **99**, 306–319.
 1060 <https://doi.org/10.1007/BF00375364>

1061 Welsch, B., Faure, F., Bachèlery, P., Famin, V., 2009. Microcrysts record transient
 1062 convection at Piton de la Fournaise volcano (La Réunion hotspot). *J. Petrol.* **50**,
 1063 2287–2305. <https://doi.org/10.1093/petrology/egp076>

1064 Wolfe, E.W., Wise, W.S., Dalrymple, G.B., 1997. The geology and petrology of Mauna Kea
 1065 Volcano, Hawaii; a study of postshield volcanism (n°1557). USGPO.,
 1066 <https://doi.org/10.3133/pp1557>

1067
 1068 **Table captions**

1069
1070
1071

1072
1073

1074

1075
1076

1077
1078

1079
1080

1081

1082
1083
1084

1085
1086
1087

1088
1089
1090
1091
1092
1093
1094
1095
1096
1097

Tab. 1 Sets of samples collected at Sites 1, 2, 3 and 4; asl: above sea level.

Tab. 2 Modal composition of samples collected at Sites 1, 2, 3 and 4. Ol: olivine, Cpx: clinopyroxene, Plg: plagioclase, Amph: amphibole, and Ox: oxides.

Tab. 3 Representative compositions for olivine at the four investigated sites.

Tab. 4 Representative compositions for clinopyroxene at the four studied sites.

Tab. 5 Representative compositions for plagioclase at the four studied sites.

Tab. 6 Representative compositions for oxides in rocks from the four investigated sites

Tab. 7 Whole-rock compositions of samples collected at Sites 1, 2, 3 and 4. L.O.I.: Loss on ignition; b.d.l.: below detection limit. Peridotite*: rock type based on hand sample descriptions.

Tab. 8 Temperatures of re-equilibration calculated with the olivine-augite Mg-Fe-exchange geothermometer of Loucks (1996). The geothermometer has a standard error of ± 6 °C.

Tab. 9 Summary of the mean characteristics of Sites 1, 2, 3 and 4

Figure captions

Fig. 1 Location maps. **a)** La Réunion Island with the massifs of Piton des Neiges (PdN) and

Piton de la Fournaise (PdF). The drill holes SLZ1 (in the cirque of Salazie) and SR1 (on the eastern flank of PdF) are indicated with yellow stars. The black rectangle indicates the studied area. **b)** Shaded relief of the cirque of Salazie. **c)** Geological map of the studied area based on our field observations, and showing the locations of the four plutonic outcrops (labeled Site 1 through 4) in the Mât River. SHI: sub-horizontal intrusion. Coordinates in UTM WGS84, zone 40S.

Fig. 2 Field characteristics observed in Sites 1, 2, 3 and 4 (see Fig. 1c for location). **a)** 2 – 2.5 cm-thick clinopyroxene- and plagioclase-rich veinlets observed in Site 1 (also observed in Site 2). **b)** Lenses of peridotites separated by mafic intrusions at Site 1 (also observed in Site 2). **c)** Overview of the outcrop in Site 2, which is crosscut and surmounted by mafic and differentiated intrusions. **d)** Example of east-dipping syn-magmatic thrust faults in Site 3. **e)** West-verging overturned folds observed in Site 3. **f)** Example of folded layering in Site 4, **g)** Layering in Site 4 through modal variations in plagioclase, olivine and clinopyroxene.

Fig. 3 Stereographic diagrams of the magmatic lineations and poles to foliation measured in Sites 3 and 4. No apparent foliation or lineation is observed at Sites 1 and 2. Stereo diagrams are equal area and lower hemisphere.

Fig. 4 Rock types sampled at Sites 1, 2, 3 and 4. N: number of samples

Fig. 5 Representative parageneses and textures of samples collected at Sites 1 and 2 (transmitted light microphotographs). **a)** Dunite from Site 1 made of anhedral grains of olivine in cumulus position, and anhedral crystals of clinopyroxene and oxides in interstitial position (sample CB4010414). **b)** Dunite from Site 2 with only olivine crystals (sample GABAMONT2). **c)** and **d)** Wehrlite samples from Sites 1 and 2, respectively, in which the olivine is euhedral and in cumulus position, and clinopyroxene is poikilitic (samples CB1010414 and GABAMONT). **e)** and **f)** Wehrlite from Site 2 made of rounded grains of olivine and euhedral, sector-zoned crystals of clinopyroxene in cumulus position, and plagioclase in interstitial position (CB4230513). **g)** and **h)** Plagioclase-wehrlites from Site 2

displaying a mesocumulate texture with euhedral olivine in cumulus position, and clinopyroxene and plagioclase in interstitial position (CB1230513). Ol: olivine, Cpx: clinopyroxene, Plg: plagioclase, Amph: amphibole and Ox: oxides.

Fig. 6 Representative parageneses and textures of samples collected at Sites 3 and 4 (transmitted-light microphotographs with crossed polars). **a)** and **b)** Olivine gabbros (samples SAL111 and CB12260513 from Sites 3 and 4, respectively), in which euhedral olivine, clinopyroxene and plagioclase show intergrowth textures. **c)** and **d)** Gabbros (samples SAL110 and CB2260513, respectively). Euhedral crystals of plagioclase and clinopyroxene **e)** and **f)** Strong magmatic fabrics, marked by elongated plagioclases in ferrogabbros (samples CB16260513 and CB2290513, respectively).

Fig. 7 Chemical composition of olivine at Sites 1, 2, 3 and 4. **a)** Fo histograms. **b)** Fo vs. CaO diagram for olivine in the layered gabbros and peridotites. See the description in the main text for populations (1), (2) and (3).

Fig. 8 Chemical compositions of clinopyroxene at Sites 1, 2, 3 and 4. **a)** Mg# histograms, **b)** Mg# vs. Cr₂O₃, and **c)** Mg# vs. Al₂O₃.

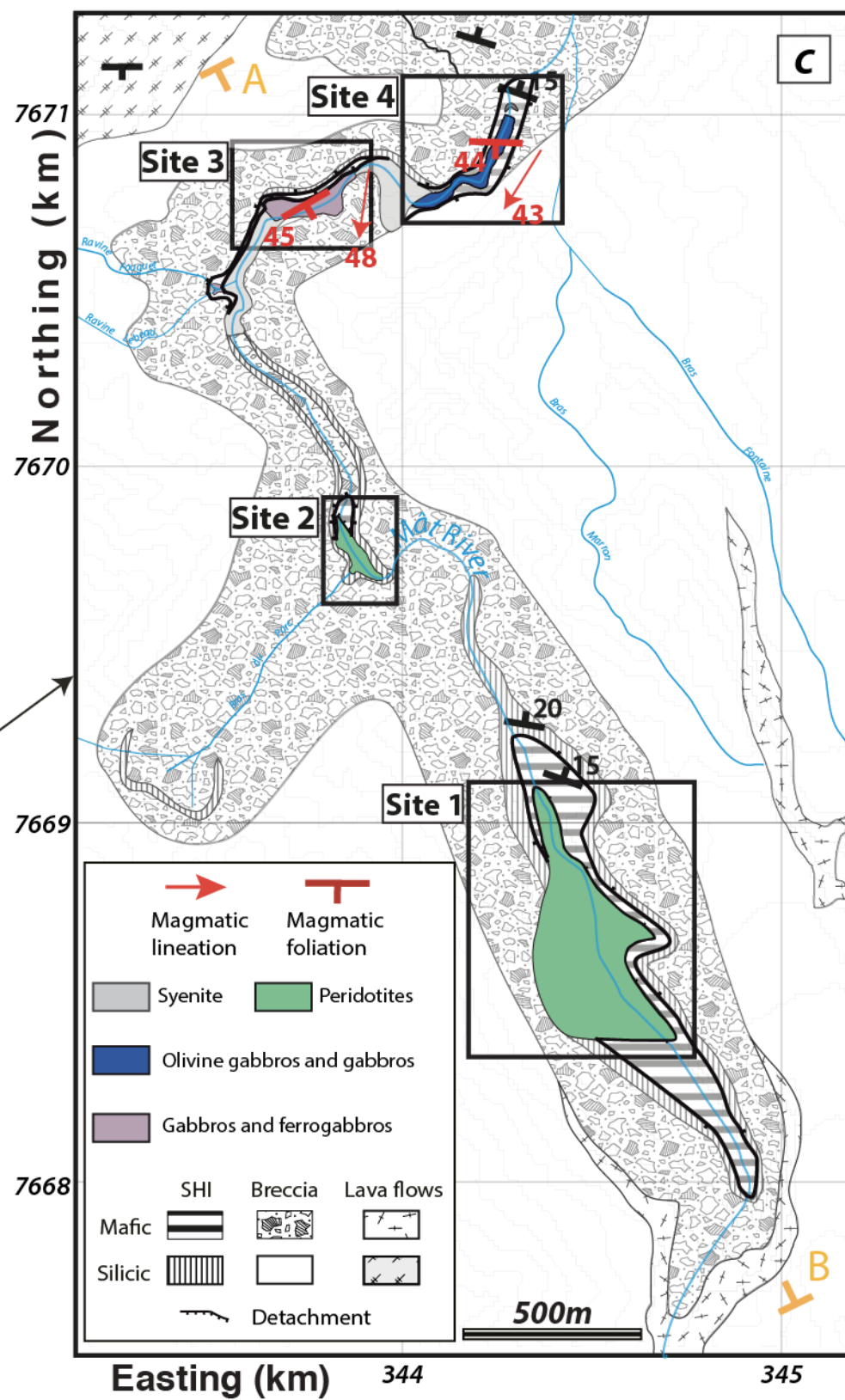
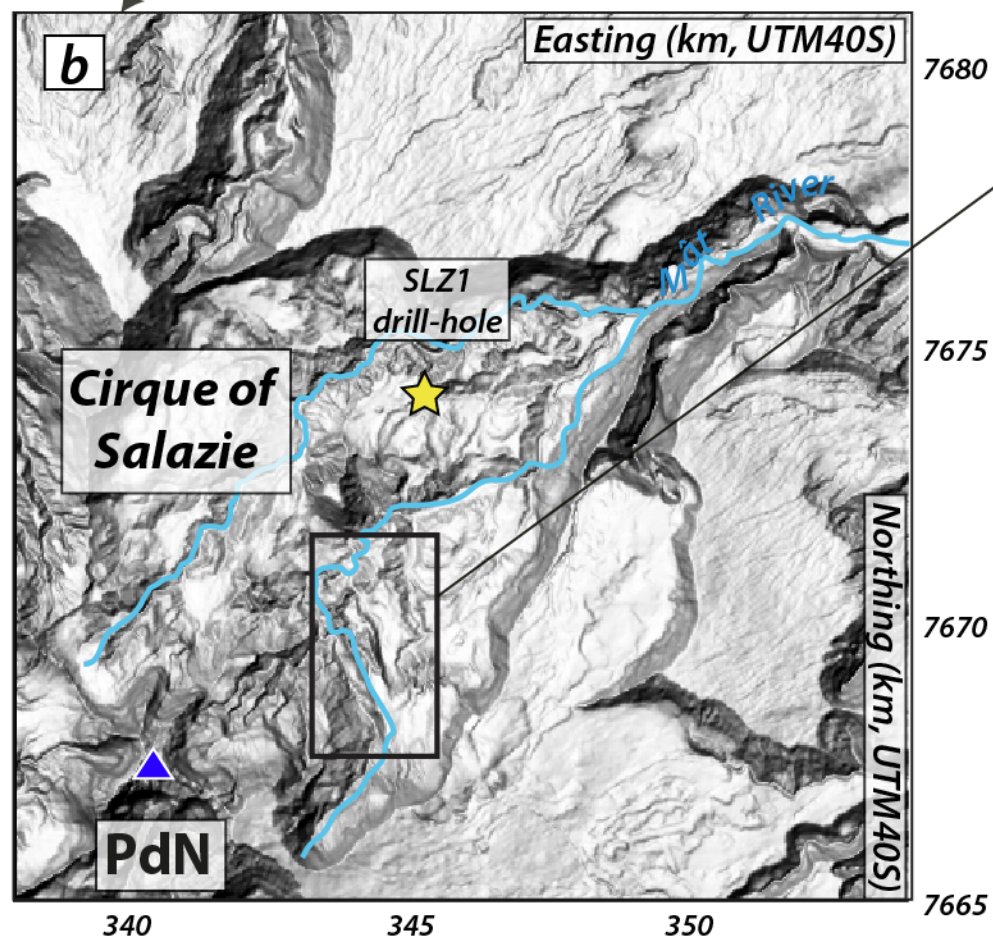
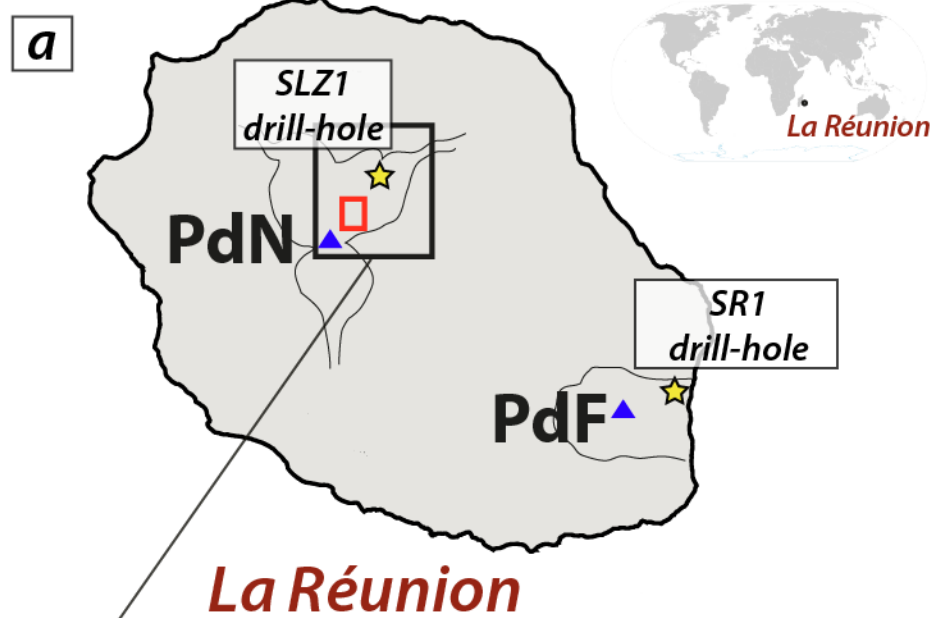
Fig. 9 Chemical compositions of plagioclase at Sites 1, 2, 3 and 4. **a)** Anorthite (An) histograms, **b)** Anorthite vs. K₂O.

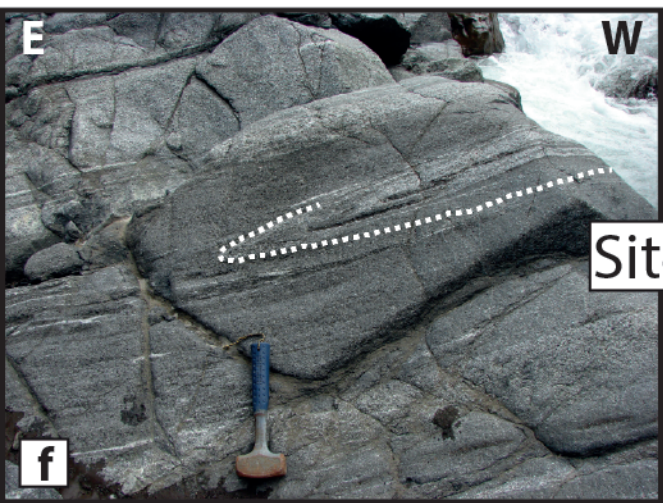
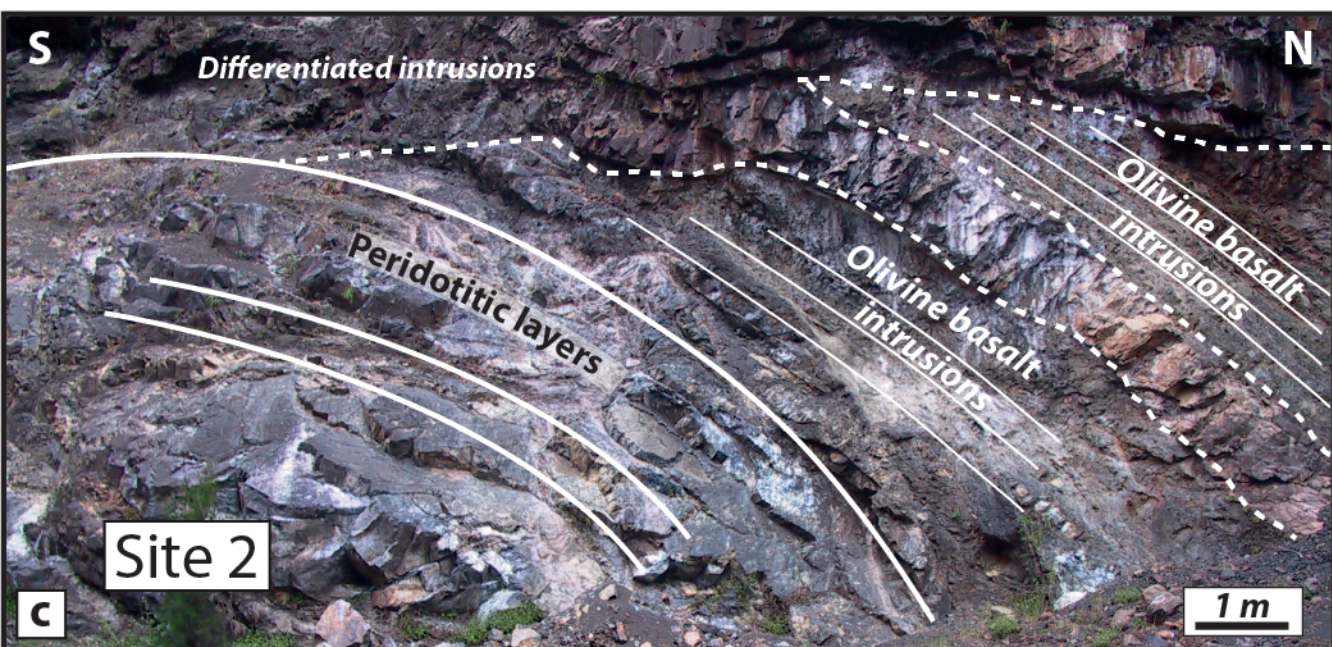
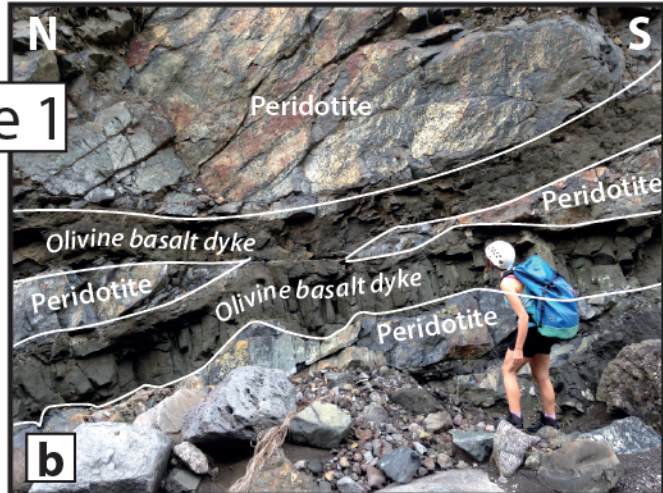
Fig. 10 Chemical compositions of oxides at Sites 1, 2, 3 and 4. **a)** Cr₂O₃ vs. FeO_t, **b)** TiO₂ vs. Al₂O₃.

Fig. 11 Whole-rock composition of samples collected at Sites 1, 2, 3 and 4. **a)** MgO vs. SiO₂. Peridotite*: rock type based on hand sample descriptions. **b)** MgO vs. CaO. **c)** SiO₂ vs. CaO. **d)** SiO₂ vs. TiO₂. **e)** Chondrite-normalized REE spider diagram (McDonough and Sun, 1995). **f)** Th vs. Sm diagram. Purple hexagon symbols represent bulk analyses of sample from Site 3 (Pronost 2001).

Fig. 12 Composition of cumulate mineral assemblages. **a)** Average Mg# for clinopyroxene plotted against Fo olivine contents, **b)** Average Mg# for oxides plotted against Fo olivine contents, **c)** Average anorthite contents versus average Mg# for clinopyroxene, **d)** Average Mg-numbers for oxide phases versus average Mg# for clinopyroxene.

Fig. 13 a) NE–SW cross section of the studied area gathering the main characteristics of each outcrop of plutonic rocks (see Fig.1c for location) and introducing our two hypotheses. The first hypothesis considers that the plutonic rocks exposed by the Mât River at Sites 1, 2, 3 and 4 correspond to different levels in the upper margin of a single magma chamber, where peridotitic layers top off gabbroic layers. In our second hypothesis, the four outcrops are parts of a multiple level magma storage feeding the volcano built by repeated injections of magma. b) Sketch of the Piton des Neiges (with vertical exaggeration of the actual topography) with the location of the four plutonic outcrops at Sites 1, 2, 3 and 4 (S1, S2, S3 and S4, respectively). We suggest that gabbroic series in Sites 3–4 belong to the magmatic system of a volcanic edifice that predated the building of Piton des Neiges (i.e. Proto-Piton des Neiges). Then, a large destabilization toward the North affected severely the magmatic system of the old volcano, and lead to a migration of the volcanic center further south for the edification of Piton des Neiges and the emplacement of peridotitic series at the Sites 1–2. EC: eruptive center. Dashed line: supposed topography of the Proto-Piton des Neiges. The presence of a high resistivity body underlying the cirque of Cilaos is revealed by geophysical data (Gailler and Lénat 2012).

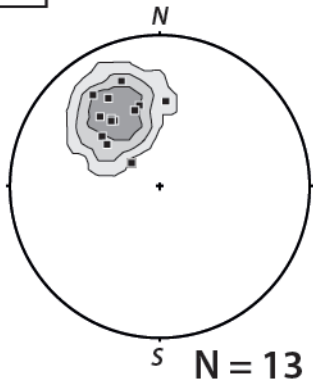
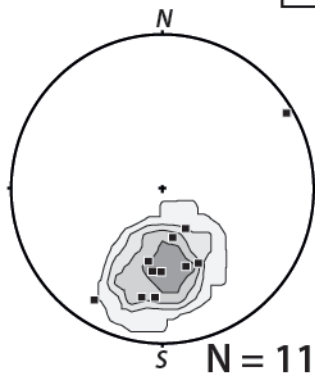




*Magmatic
lineation*

Site 3

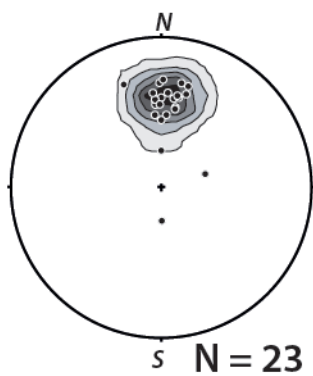
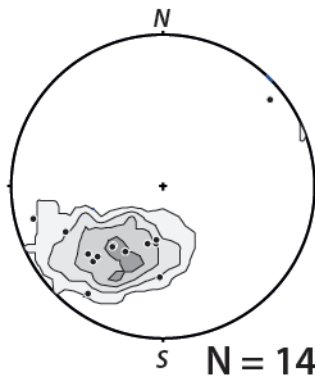
*Magmatic
foliation*



*Magmatic
lineation*

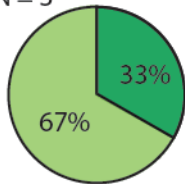
Site 4

*Magmatic
foliation*



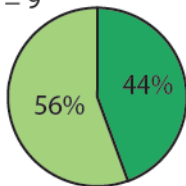
Site 1

N = 3



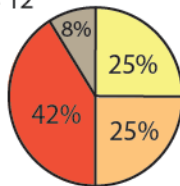
Site 2

N = 9



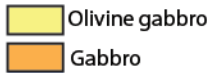
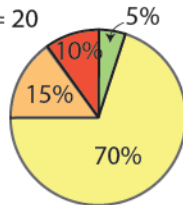
Site 3

N = 12

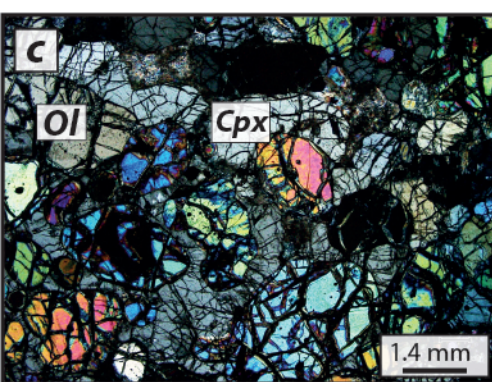
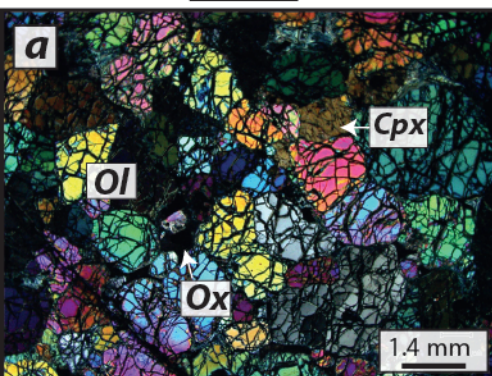


Site 4

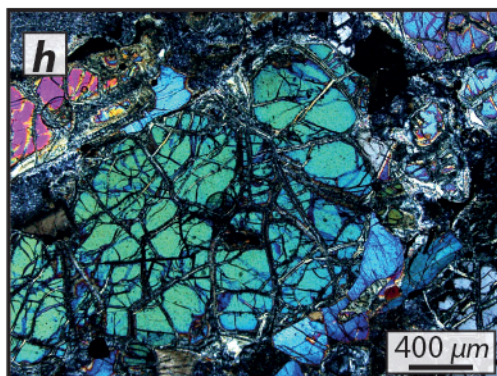
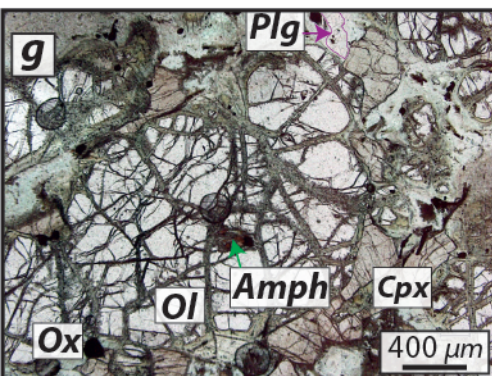
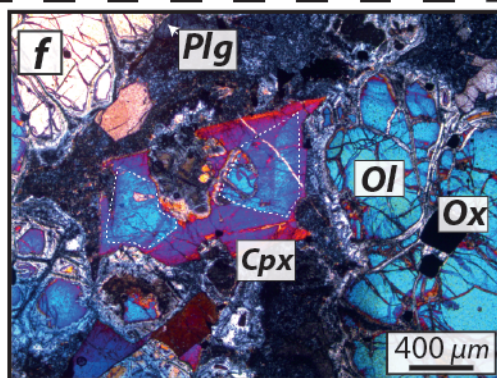
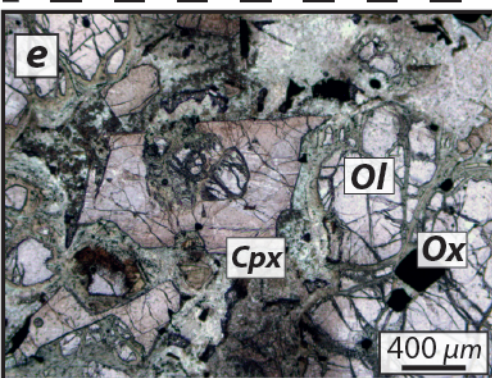
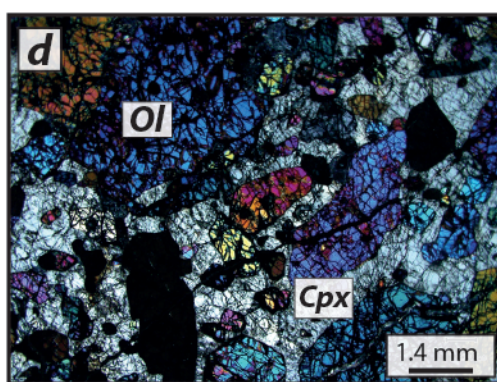
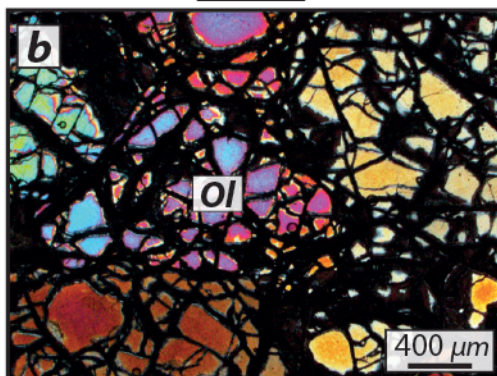
N = 20



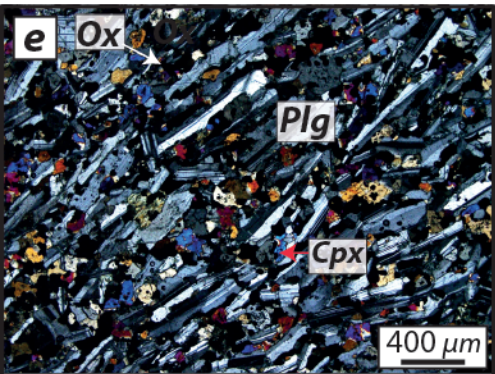
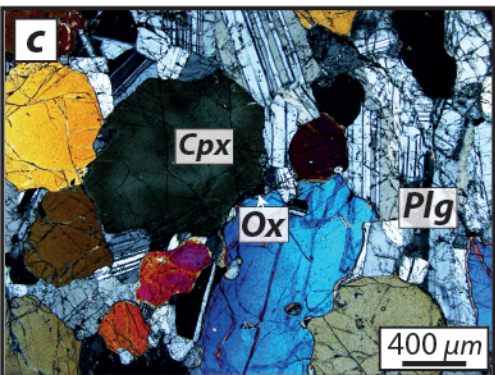
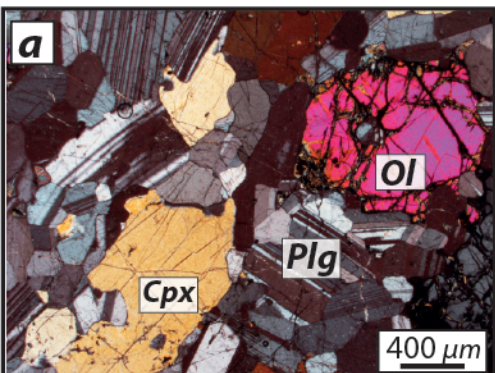
Site 1



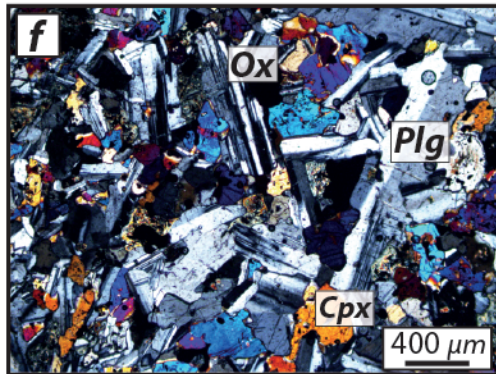
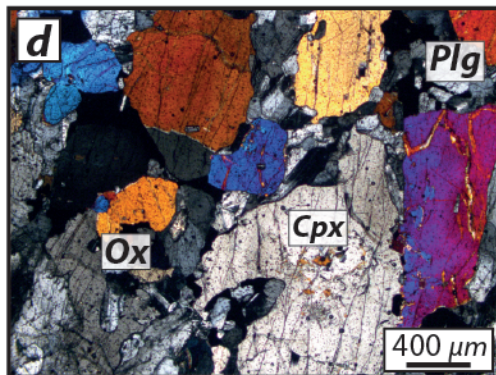
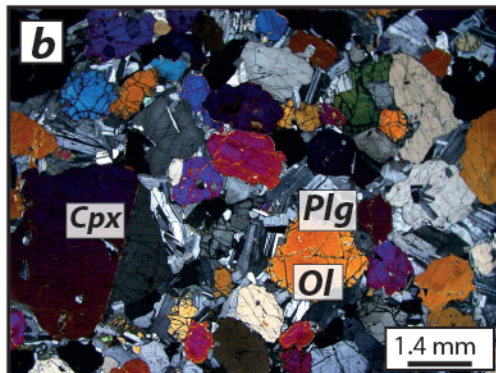
Site 2

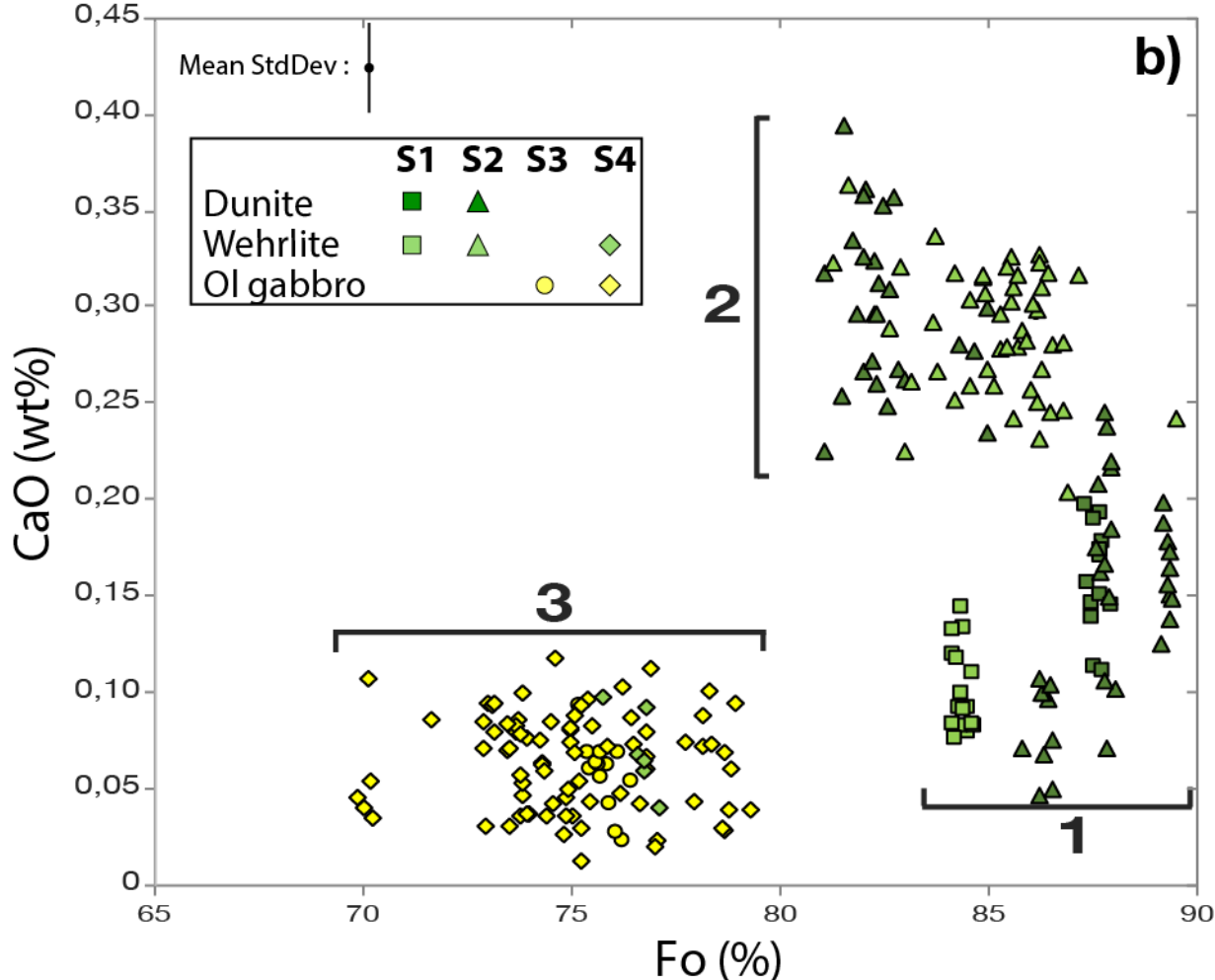
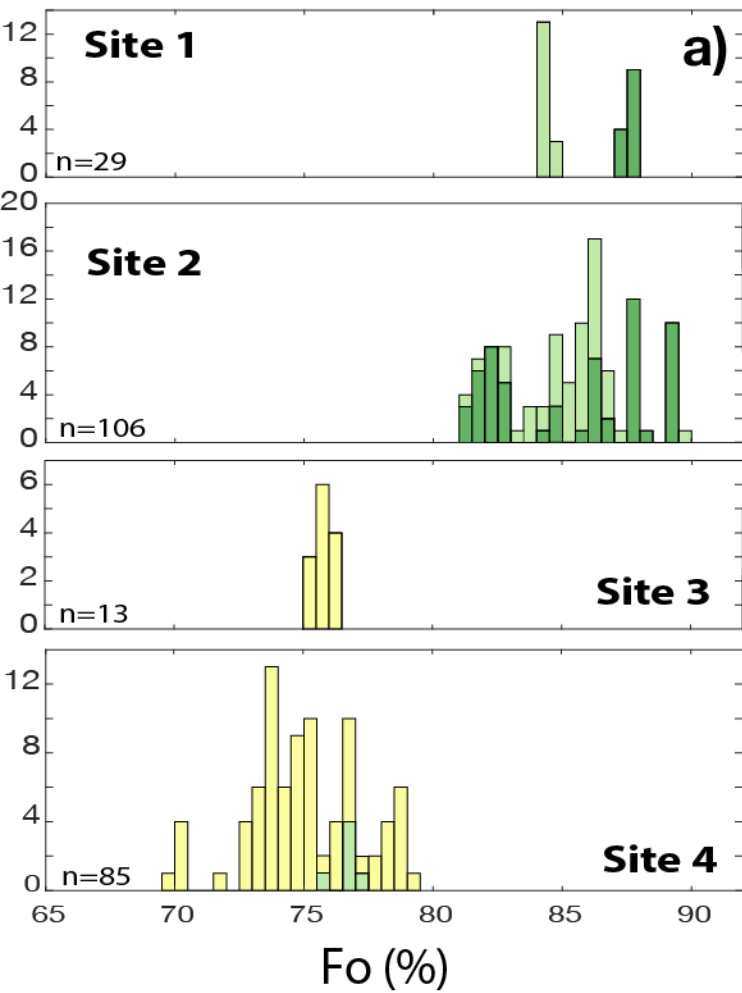


Site 3

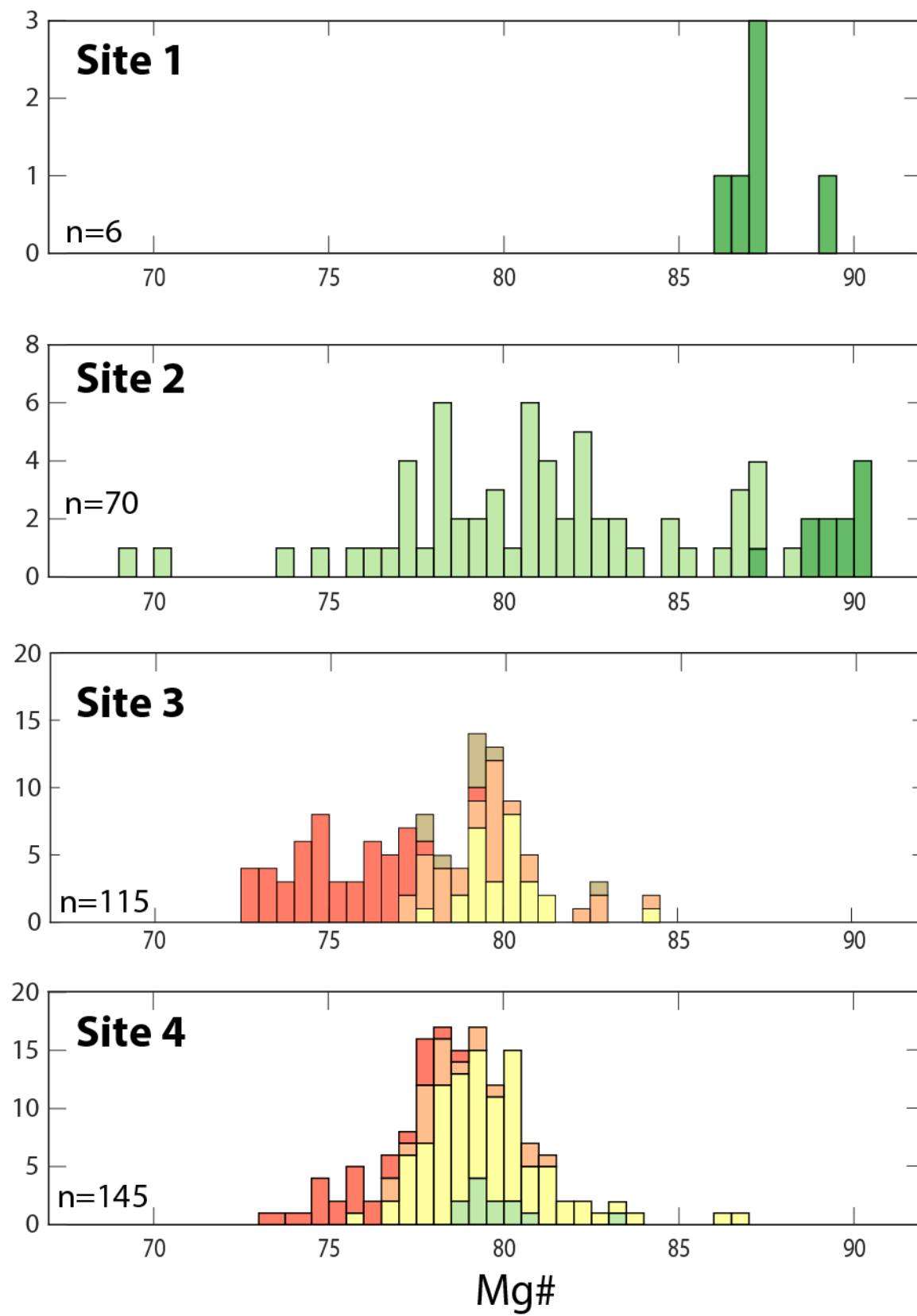


Site 4

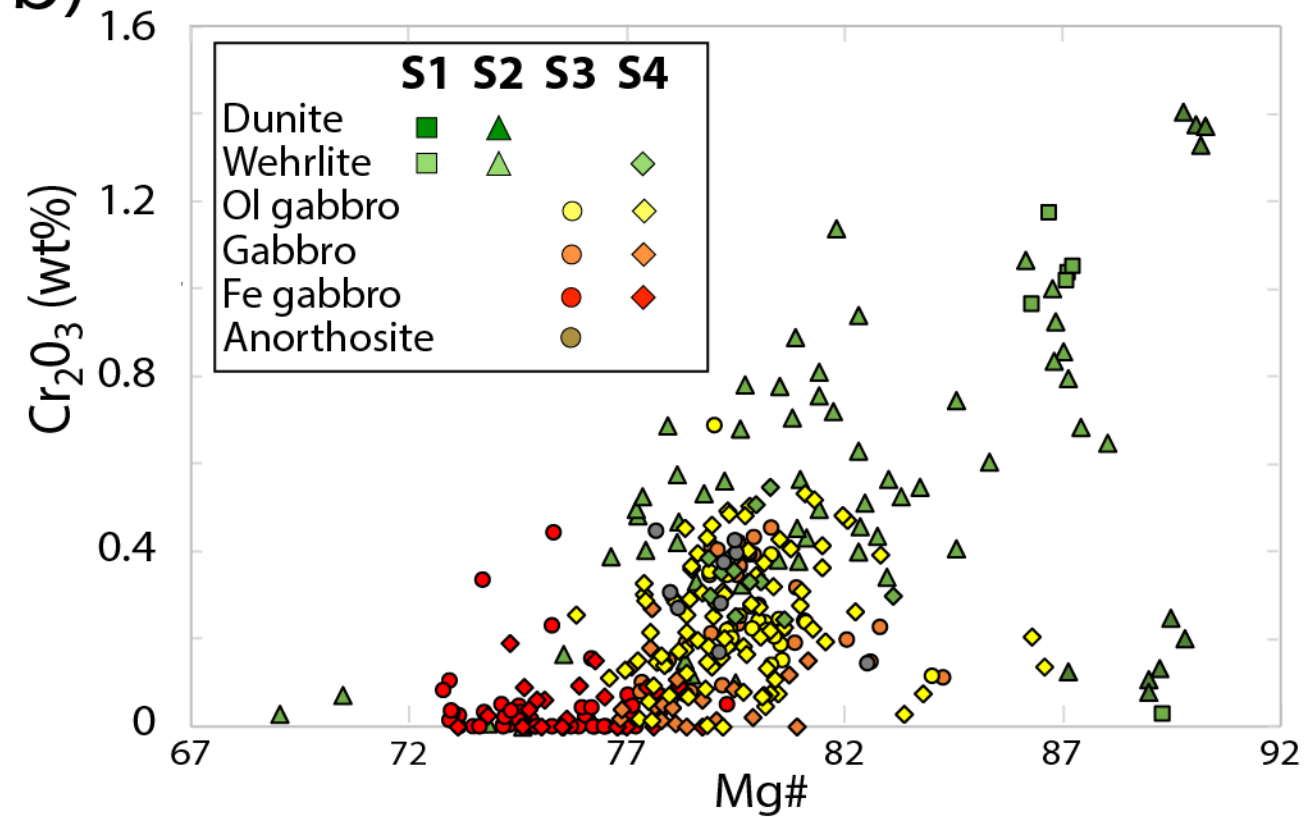




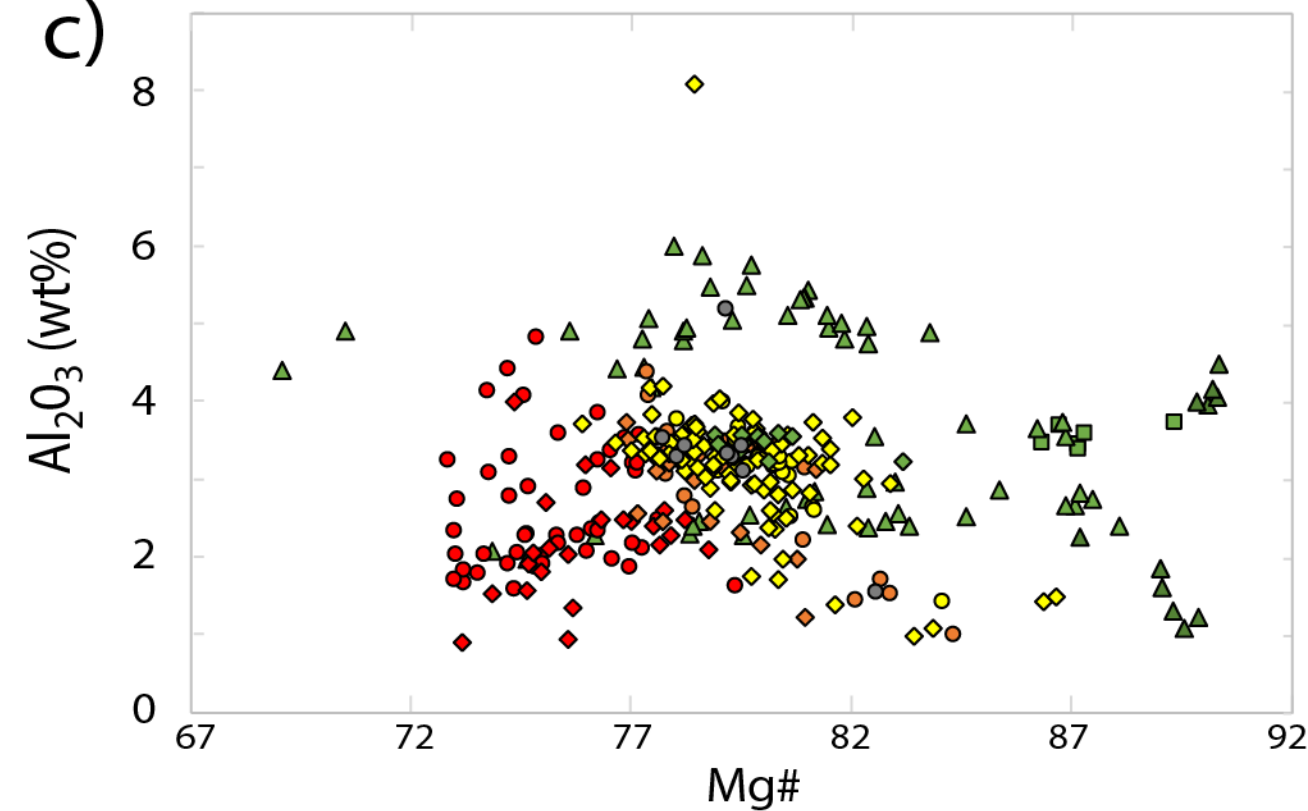
a)

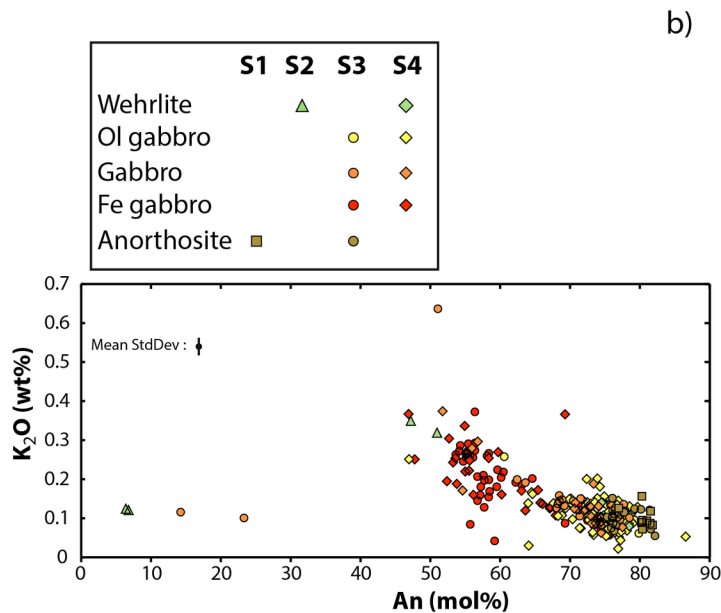
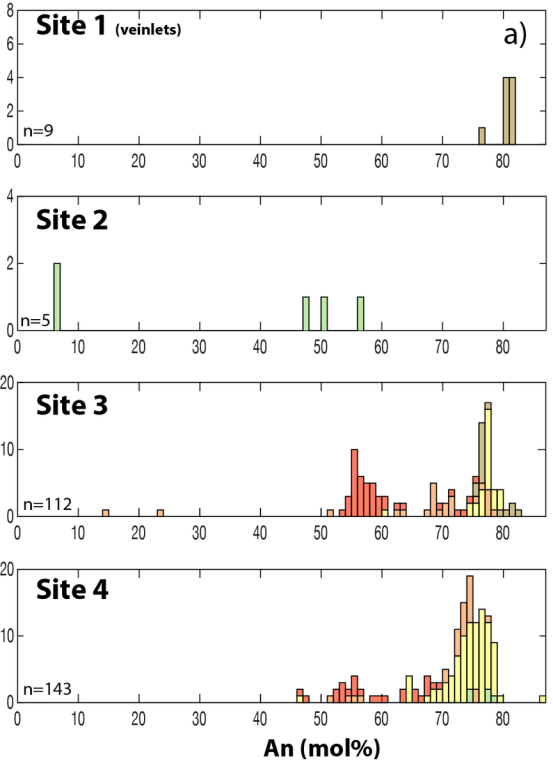


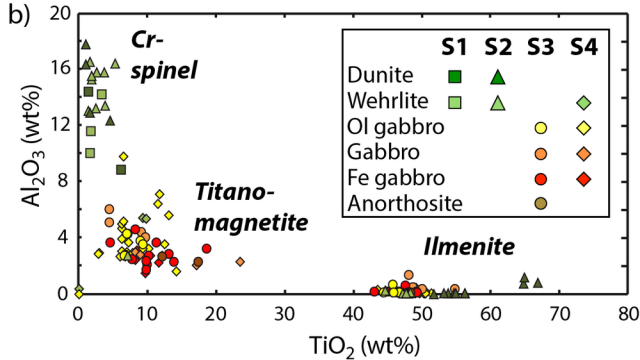
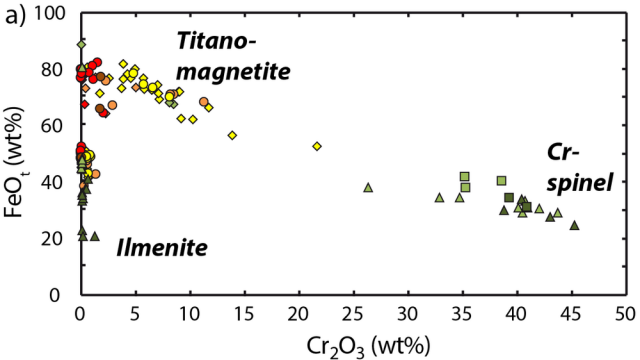
b)

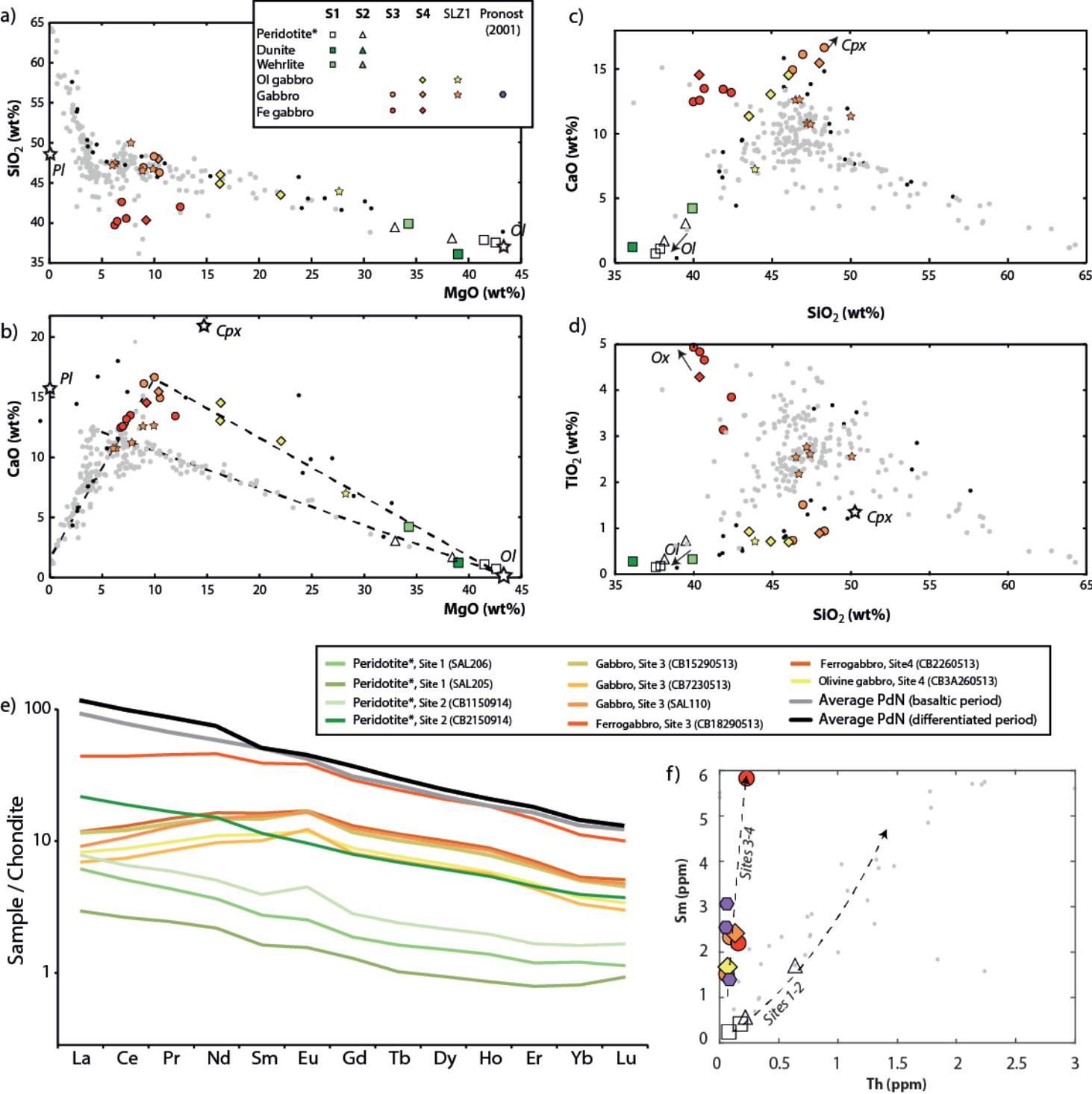


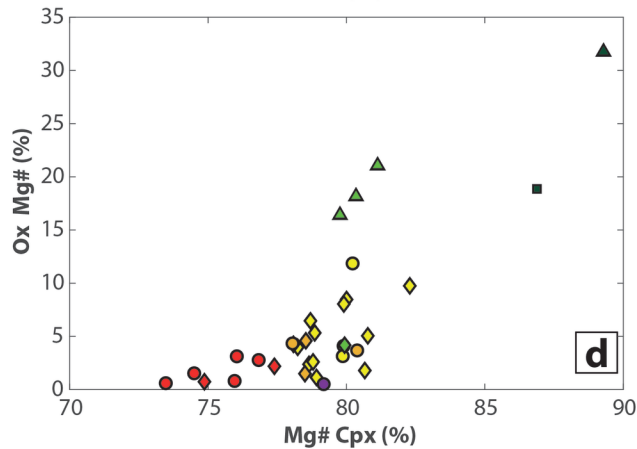
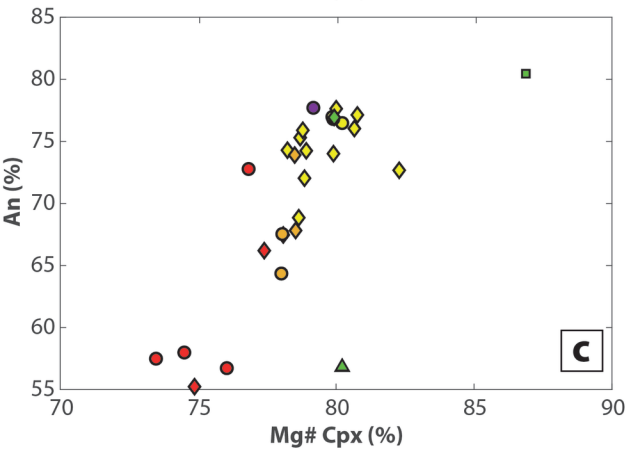
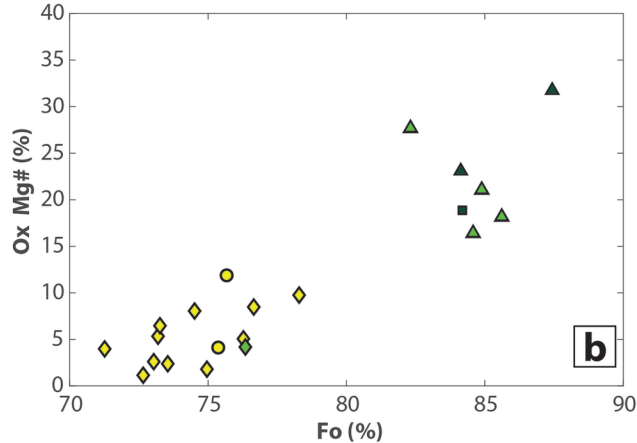
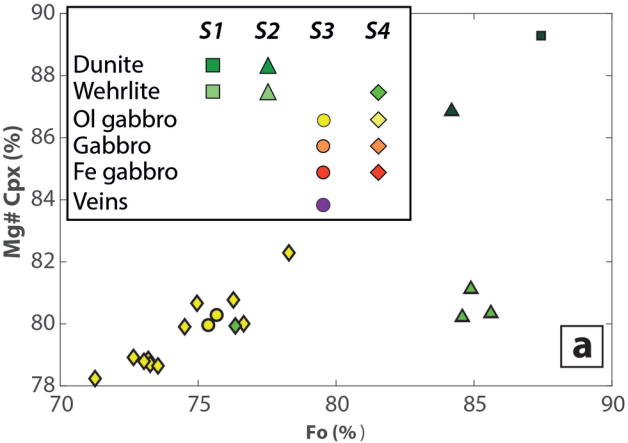
c)

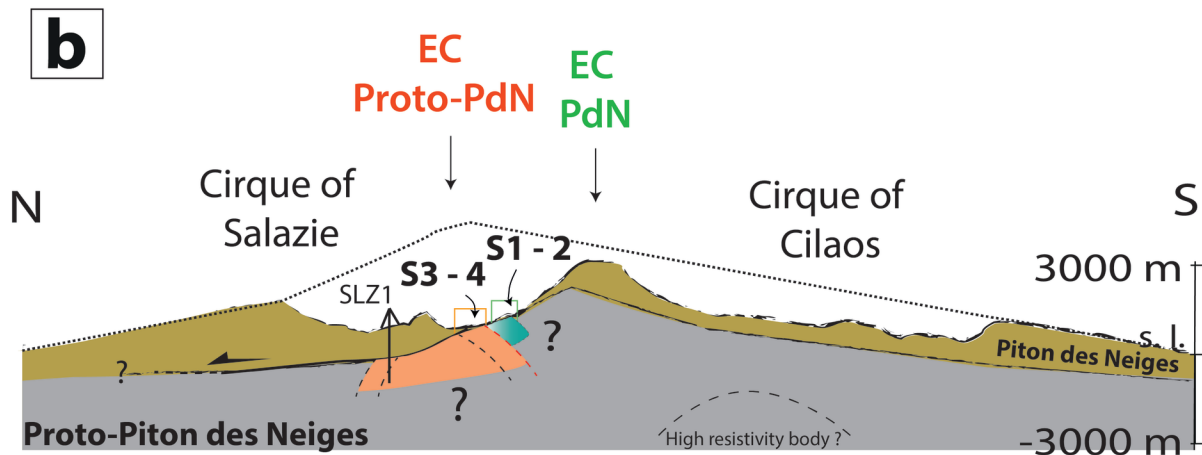
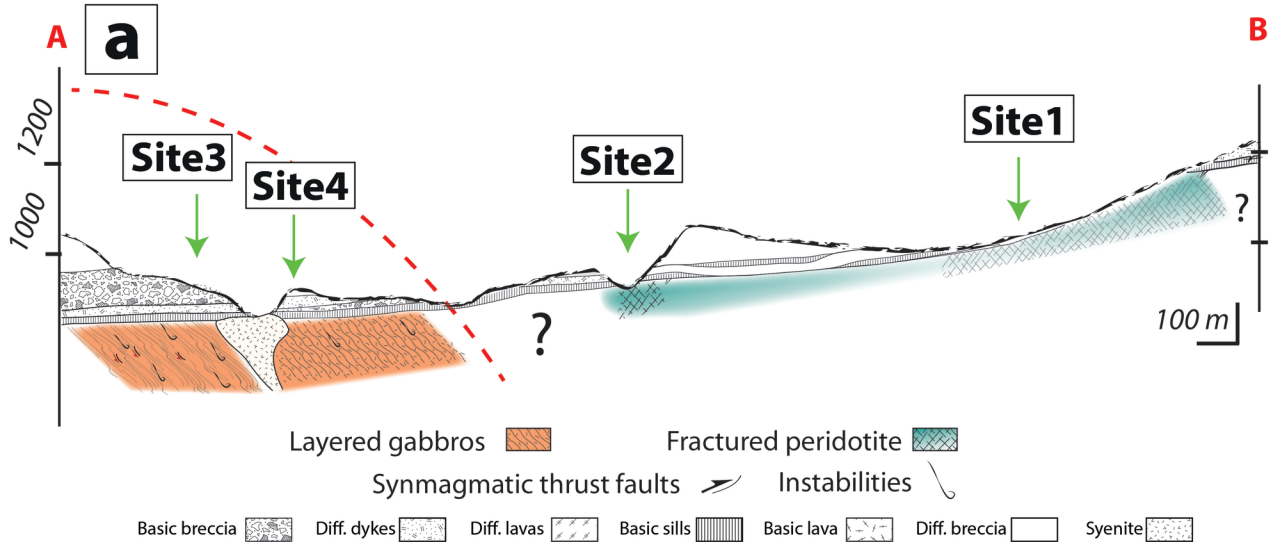












Sample name	Rock type	Texture	Ol (vol%)	Cpx (vol%)	Plg (vol%)	Ox (vol%)	Amph (vol%)
<u>Site 1</u>							
CB1010414	Wehrlite	Adcumulate	70	15	10*	5	-
CB2010414	Wehrlite	Adcumulate	56	40	0	4	-
CB4010414	Dunite	Adcumulate	94	5	0	1	-
<u>Site 2</u>							
<i>gabamont</i>	Wehrlite	Heteradcumulate	80	19	0	1	-
<i>gabamont2</i>	Dunite	Adcumulate	100	0	0	0	-
<i>gabamont1</i>	Wehrlite	Heteradcumulate	70	30	< 1	0	-
CB1230513	Plg-Wehrlite	Mesocumulate	65	25	8	2	-
CB2230513	Wehrlite	Mesocumulate	60	34	4	2	-
CB4230513	Wehrlite	Mesocumulate	74	25	0	1	-
CB1	Dunite	Adcumulate	80	5	0	5	10
CB26	Dunite	Adcumulate	98	0	0	2	-
CB36	Dunite	Adcumulate	98	0	0	2	-
<u>Site 3</u>							
CB15290513	<i>Gabbro</i>	Mesocumulate	0	80	20	0	-
CB16290513	<i>Ferrogabbro</i>	Mesocumulate	0	35	40	25	-
CB17290513	<i>Ferrogabbro</i>	Mesocumulate	0	30	45	25	-
CB18290513	<i>Ferrogabbro</i>	Mesocumulate	0	35	40	25	-
CB61	<i>Ol-gabbro</i>	Mesocumulate	35	40	20	5	-
CB57*	<i>Anorthosite</i>	Adcumulate	0	3	96	1	-
CB55	<i>Ol-gabbro</i>	Mesocumulate	35	40	20	5	-
SAL110	<i>Gabbro</i>	Mesocumulate	0	44	54	2	-
SAL111	<i>Ol-gabbro</i>	Mesocumulate	15	50	35	0	-
CB5230513	<i>Ferrogabbro</i>	Mesocumulate	15	25	40	20	-
CB6230513	<i>Ferrogabbro</i>	Mesocumulate	0	50	40	10	-
CB7230513	<i>Gabbro</i>	Mesocumulate	0	60	40	< 1	-
<u>Site 4</u>							
CB1290513	Wehrlite	Adcumulate	55	33	5	7	-
CB2290513	<i>Ferrogabbro</i>	Mesocumulate	0	50	43	7	-
CB3290513	<i>Ol-gabbro</i>	Mesocumulate	34	50	15	1	-
CB14260513	<i>Ol-gabbro</i>	Mesocumulate	15	45	39	1	-
CB13260513	<i>Ol-gabbro</i>	Mesocumulate	10	49	40	1	-
CB12260513	<i>Ol-gabbro</i>	Mesocumulate	15	50	35	0	-
CB11260513	<i>Ol-gabbro</i>	Mesocumulate	2	55	40	3	-
CB10260513	<i>Ol-gabbro</i>	Mesocumulate	35	49.5	15	0.5	-
CB9260513	<i>Gabbro</i>	Adcumulate	0	59	40	1	-
CB8260513	<i>Ol-gabbro</i>	Adcumulate to mesocumulate	34	40	25	1	-
CB6260513	<i>Ol-gabbro</i>	Mesocumulate	28	55	15	2	-
CB5260513	<i>Ol-gabbro</i>	Mesocumulate	10	40	49	1	-
CB4260513	<i>Ol-gabbro</i>	Mesocumulate	15	40	45	0	-
CB3b260513	<i>Ol-gabbro</i>	Mesocumulate	45	39	15	1	-
CB3a260513	<i>Ol-gabbro</i>	Mesocumulate	25	45	30	0	-
CB2260513	<i>Gabbro</i>	Mesocumulate	0	45	50	5	-
CB1260513	<i>Ferrogabbro</i>	Mesocumulate	0	30	45	25	-
CB105	<i>Gabbro</i>	Mesocumulate	0	54	45	1	-
CB100	<i>Ol-gabbro</i>	Mesocumulate	10	50	40	0	-
CB99	<i>Ol-gabbro</i>	Mesocumulate	20	50	30	0	-

* Vein

Rock type	Dunite		Wehrlite		Olivine gabbro	
Site	<i>S1</i>	<i>S2</i>	<i>S1</i>	<i>S4</i>	<i>S3</i>	<i>S4</i>
Sample	<i>CB4010414</i>	<i>Gabamont2</i>	<i>CB1010414</i>	<i>CB1290513</i>	<i>CB55</i>	<i>CB3B260513</i>
	Olivine	Olivine	Olivine	Olivine	Olivine	Olivine
SiO2	40.04	40.48	39.46	39.12	38.31	38.97
TiO2	0.01	0.06	0.06	0.00	0.00	0.00
Al2O3	0.04	0.03	0.01	0.03	0.04	0.02
Cr2O3	0.04	0.00	0.04	0.04	0.01	0.03
FeOt	11.48	11.13	14.43	20.70	22.11	19.50
MnO	0.26	0.16	0.18	0.29	0.34	0.33
MgO	47.72	46.90	44.80	39.37	38.51	40.71
CaO	0.15	0.22	0.08	0.04	0.06	0.04
Na2O	0.00	0.00	0.00	0.00	0.00	0.00
K2O	0.00	0.00	0.00	0.00	0.00	0.00
NiO	–	0.41	–	0.20	–	0.23
Total	99.74	99.38	99.07	99.80	99.38	99.84
Fo (mol%)	87.9	88.0	84.6	77.1	75.6	78.8

Rock type	Wehrlite		Olivine gabbro		Gabbro		Ferrogabbro		Anorthosite
Site	S1	S2	S3	S4	S3	S4	S3	S4	S3
Sample	CB1010414	CB1230513	SAL111	CB12260513	SAL110	CB2260513	CB18290513	CB1260513	CB57
	Clinopyroxene	Clinopyroxene	Clinopyroxene	Clinopyroxene	Clinopyroxene	Clinopyroxene	Clinopyroxene	Clinopyroxene	Clinopyroxene
SiO2	51.19	51.80	50.84	50.32	50.69	53.12	52.04	52.53	50.73
TiO2	1.12	0.90	1.40	1.32	1.42	0.26	0.71	0.54	1.49
Al2O3	3.58	2.55	3.28	3.77	2.76	1.20	1.96	1.51	3.27
Cr2O3	1.05	0.57	0.24	0.48	0.08	0.00	0.00	0.03	0.37
FeOt	4.26	5.93	6.79	6.80	7.29	6.49	8.16	9.29	7.00
MnO	0.14	0.14	0.15	0.12	0.19	0.24	0.40	0.31	0.12
MgO	16.34	16.25	15.25	14.98	14.64	15.43	14.93	14.70	14.99
CaO	21.88	21.12	21.58	21.57	21.74	23.01	21.63	20.92	22.08
Na2O	0.29	0.21	0.30	0.37	0.38	0.21	0.36	0.32	0.38
K2O	0.00	0.00	0.01	0.01	0.00	0.00	0.00	0.02	0.00
NiO	—	0.04	0.03	0.04	0.04	0.00	0.00	0.00	—
Total	99.85	99.51	99.85	99.79	99.23	99.96	100.21	100.17	100.42
Wo (%)	45.5	43.6	44.8	45.1	45.3	46.3	44.1	42.8	45.5
En (%)	47.3	46.6	44.0	43.6	42.5	43.2	42.3	41.9	43.0
Fs (%)	6.9	9.5	11.0	11.1	11.9	10.2	13.0	14.8	11.3
Mg#	87.2	83.0	80.0	79.7	78.2	80.9	76.5	73.8	79.3

Rock type	Wehrlite		Olivine gabbro		Gabbro		Ferrogabbro		Anorthosite
Site	S1	S2	S3	S4	S3	S4	S3	S4	S3
Sample	CB1010414	CB1230513	SAL111	CB12260513	SAL110	CB2260513	CB16290513	CB1260513	CB57
	Plagioclase	Plagioclase	Plagioclase	Plagioclase	Plagioclase	Plagioclase	Plagioclase	Plagioclase	Plagioclase
SiO2	48.41	54.04	48.88	48.17	50.57	50.22	54.40	54.08	48.28
TiO2	0.05	0.11	0.08	0.08	0.00	0.02	0.02	0.09	0.12
Al2O3	31.90	27.73	32.17	32.43	30.51	30.89	28.67	28.34	32.22
Cr2O3	0.01	0.00	0.00	0.03	0.00	0.00	0.01	0.00	0.00
FeOt	0.37	0.73	0.43	0.38	0.43	0.34	0.33	0.54	0.46
MnO	0.02	0.04	0.00	0.03	0.00	0.02	0.00	0.00	0.03
MgO	0.06	0.12	0.04	0.05	0.04	0.02	0.02	0.03	0.03
CaO	15.52	11.62	15.54	16.12	14.14	14.39	11.27	11.64	16.40
Na2O	2.48	4.68	2.61	2.35	3.43	3.22	4.90	5.00	2.29
K2O	0.13	0.29	0.11	0.13	0.15	0.13	0.26	0.22	0.12
Total	98.95	99.83	99.87	99.79	99.27	99.25	99.92	99.96	99.96
An (mol%)	77.0	56.8	76.2	78.5	68.9	70.6	55.2	55.6	79.3

Rock type	<u>Site 1</u>				<u>Site 2</u>		<u>Site 3</u>								<u>Site 4</u>				
	Dunite	WerlHITE	Peridotite*	Peridotite*	Peridotite*	Peridotite*	Fe-gabbro	Gabbro	Fe-gabbro	Fe-gabbro	Gabbro	Fe-gabbro	Fe-gabbro	Gabbro	Ol-gabbro	Ol-gabbro	Ol-gabbro	Gabbro	Fe-gabbro
Sample	CB4010414	CB1010414	SAL206	SAL205	CB1150914	CB2150914	CB16290513	CB15290513	CB1230914	CB18290513	SAL110	CB5230513	CB6230513	CB7230513	CB12260513	CB3A260513	CB8260513	CB9260513	CB2260513
(wt%)																			
SiO2	36.11	39.92	37.88	37.57	38.13	39.49	39.98	48.31	42.39	40.38	46.94	40.67	41.88	46.30	46.04	44.90	43.52	48.00	40.36
Al2O3	1.14	4.02	1.38	0.68	2.67	3.64	12.80	14.12	13.562	12.81	14.57	12.91	10.66	15.96	10.72	10.92	5.54	13.45	10.93
Fe2O3	10.67	12.30	11.35	12.36	11.28	13.64	18.36	6.38	15.875	18.90	8.38	18.02	16.41	6.73	9.18	10.12	14.87	6.03	18.18
MnO	0.14	0.16	0.15	0.16	0.15	0.18	0.25	0.11	0.2027	0.24	0.12	0.24	0.20	0.10	0.14	0.15	0.20	0.10	0.18
MgO	38.99	34.26	41.47	42.58	38.41	32.96	6.75	9.97	7.303	6.94	8.96	7.66	11.96	10.49	16.30	16.25	22.06	10.37	9.22
CaO	1.23	4.23	1.11	0.72	1.72	3.07	12.48	16.66	13.183	12.58	16.14	13.50	13.44	14.94	14.54	13.04	11.36	15.47	14.55
Na2O	0.05	0.44	0.05	0.01	0.06	0.27	1.94	1.69	2.051	2.05	1.65	1.67	0.87	1.29	0.81	0.87	0.41	1.75	1.05
K2O	0.04	0.04	0.04	0.01	0.07	0.15	0.11	0.37	0.163	0.11	0.20	0.10	0.06	0.60	0.11	0.09	0.03	0.51	0.09
TiO2	0.28	0.33	0.18	0.16	0.34	0.74	4.93	0.94	3.849	4.83	1.51	4.65	3.14	0.74	0.70	0.72	0.93	0.89	4.28
P2O5	0.05	0.04	0.04	0.04	0.04	0.10	0.80	b.d.l.	0.34	0.47	b.d.l.	0.61	b.d.l.	b.d.l.	b.d.l.	b.d.l.	b.d.l.	b.d.l.	b.d.l.
L.O.I.	9.84	4.60	5.19	4.50	6.52	4.68	0.37	1.76	0.86	0.85	1.28	0.63	2.06	2.73	1.17	1.47	1.29	2.25	0.53
Total	98.54	100.34	98.84	98.79	99.39	98.91	98.77	100.31	99.77	100.15	99.75	100.64	100.67	99.88	99.71	98.53	100.20	98.82	99.36
(p.p.m.)																			
La			1.47	0.70	1.87	5.19		2.76		10.53	2.17			1.65		1.96			2.81
Ce			3.13	1.62	4.04	11.64		7.46		27.22	6.58			4.58		5.42			8.02
Pr			0.41	0.23	0.55	1.56		1.27		4.24	1.20			0.80		0.92			1.39
Nd			1.68	1.00	2.32	6.95		6.82		21.15	6.84			4.48		5.06			7.54
Sm			0.41	0.24	0.59	1.71		2.20		5.81	2.32			1.50		1.67			2.42
Eu			0.14	0.09	0.25	0.55		0.95		2.17	0.93			0.70		0.67			0.96
Gd			0.37	0.26	0.56	1.59		2.33		5.81	2.49			1.62		1.77			2.62
Tb			0.06	0.04	0.09	0.25		0.37		0.89	0.40			0.26		0.28			0.41
Dy			0.37	0.23	0.53	1.51		2.24		5.16	2.37			1.54		1.66			2.50
Ho			0.08	0.05	0.11	0.30		0.43		1.01	0.47			0.31		0.32			0.49
Er			0.19	0.13	0.27	0.73		1.02		2.37	1.08			0.70		0.77			1.13
Yb			0.20	0.13	0.26	0.64		0.82		1.81	0.83			0.54		0.61			0.86
Lu			0.03	0.02	0.04	0.09		0.11		0.25	0.12			0.07		0.08			0.13
Th			0.18	0.08	0.22	0.64		0.16		0.23	0.09			0.06		0.07			0.13
Sc			7.27	6.22	8.26	13.53		56.59		35.75	50.64			48.62		43.28			55.34
Ni			2112	2215	2016	1415		201		48	141			224		421			164

Sample	Rock type	(Fe/Mg) _{cpx}	(Fe/Mg) _{ol}	K _D ^(Ol/Aug)	T (°C)
Site 1					
CB1010414	Wehrlite	0.129	0.177	1.371	1165
Site 2					
CB4230513 [#]	Wehrlite	0.178	0.171	0.960	1275
CB2230513 [#]	Wehrlite	0.182	0.160	0.880	1278
CB1230513 [#]	Wehrlite	0.203	0.175	0.861	1279
CB1	Dunite	0.103	0.157	1.526	1130
Site 3					
SAL111	Ol-gabbro	0.199	0.315	1.584	1118
CB55	Ol-gabbro	0.192	0.320	1.665	1100
Site 4					
CB1290513	Wehrlite	0.185	0.304	1.646	1105
CB3290513	Ol-gabbro	0.185	0.299	1.615	1110
CB12260513	Ol-gabbro	0.180	0.305	1.693	1095
CB13260513	Ol-gabbro	0.214	0.360	1.684	1093
CB8260513	Ol-gabbro	0.170	0.328	1.926	1039
CB6260513	Ol-gabbro	0.196	0.358	1.824	1062
CB5260513	Ol-gabbro	0.221	0.353	1.596	1116
CB4260513	Ol-gabbro	0.222	0.361	1.624	1109
CB3b260513	Ol-gabbro	0.163	0.272	1.671	1098
CB3a260513	Ol-gabbro	0.209	0.335	1.602	1113
CB100	Ol-gabbro	0.223	0.370	1.661	1115
CB99	Ol-gabbro	0.227	0.396	1.741	1081
[#] Ol and cpx in disequilibrium (cf. Fig. 5e-h)					

B (SE)**A (NW)**

<i>Characteristics</i>	Site 1		Site 2		Site 4		Site 3
<u>Altitude</u>	950-1200m a.s.l.		850-940m a.s.l.		660-750m a.s.l.		750-870m a.s.l.
<u>Field work</u>							
<i>Structural characteristics</i>	Lenses and stratifications, no dynamic structure	----	Layered, some dynamic structures	----	Layered, numerous dynamic structures		
<u>Petrology</u>							
<i>Dominante Paragenese</i>	Dunite and werhlite	----	Olivine gabbro	----	Ferrogabbro		
<u>Geochemistry</u>							
MgO (wt%)	42.3	----	38.7	/	15.1	----	8.9
Na ₂ O (wt%)	0.14	----	0.16	----	0.98	----	1.65
Eu(ppm)	0.12	----	0.4	----	0.8	----	1.19
Ni(ppm)	2164	----	1716	/	293	----	154
Sc(ppm)	6.7	----	10.9	/	49.3	----	47.9
<u>Minerals composition</u>							
Ol Fo (%)	85.6	----	85.2	/	74.8	----	75.5
Cpx Mg# (%)	87.3	----	81.4	----	78.9	----	77.8
Plg An (%)	80.5	?	16.8*	?	71.0	----	67.8
Ox Mg# (%)	24.9	----	26.4	----	4.7	----	2.9

---- = Continuum

/ = Gap

* = Interstitial plagioclases